Redirected tropisms of extracellular vesicles and exomeres yield distinct biodistribution profiles

Anthony Yan-Tang Wu[+,□,⍰], Yun-Chieh Sung[&,$], Steven Ting-Yu Chou[+], Vanessa Guo[+], Jasper Che-Yung Chien[+], John Jun-Sheng Ko[+], Alan Ling Yang[+], Ju-Chen Chuang[+], Hsi-Chien Huang[&,$], Ysuan Wu[+], Meng-Ru Ho[@], Maria Ericsson[!], Wan-Wan Lin[□,⍰], Chantal Hoi Yin Cheung[++], Hsueh-Fen Juan[++,%], Koji Ueda[#], Yunching Chen[&], Charles Pin-Kuang Lai[+,□,%,*]

Affiliations:

[+]Institute of Atomic and Molecular Sciences, Academia Sinica, Taipei, Taiwan

[□]Chemical Biology and Molecular Biophysics Program, Taiwan International Graduate Program, Academia Sinica, Taipei, Taiwan

[⍰]Department of Pharmacology, College of Medicine, National Taiwan University, Taipei, Taiwan

[%]Genome and Systems Biology Degree Program, National Taiwan University and Academia Sinica, Taipei, Taiwan.

[&]Institute of Biomedical Engineering and Frontier Research Center on Fundamental and Applied Sciences of Matters, National Tsing Hua University, Hsinchu, Taiwan

[$]Department of Chemical Engineering, National Tsing Hua University, Hsinchu, Taiwan

[++]Department of Life Science, National Taiwan University, Taipei, Taiwan

[#]Cancer Proteomics Group, Cancer Precision Medicine Center, Japanese Foundation for Cancer Research, Tokyo, Japan

[@]Institute of Biological Chemistry, Academia Sinica, Taipei, Taiwan

[!]Department of Cell Biology, Harvard Medical School, Boston, Massachusetts, USA

Keywords: Extracellular vesicles, bioluminescence resonance energy transfer, exosomes, exomeres, microvesicles, redirected tropism, biodistribution, super-resolution imaging

Abstract

Bionanoparticles including extracellular vesicles and exomeres (collectively termed EVs), have been shown to play significant roles in diseases and therapeutic applications. However, their spatiotemporal dynamics *in vivo* have remained largely unresolved in detail due to the lack of a suitable method. Here we report the development of a multi-resolution EV reporter, and reveal distinct biodistribution profiles following redirection of EV tropisms. We created a bioluminescence resonance energy transfer (BRET)-based reporter, PalmGRET, to enable pan-bionanoparticle labelling ranging from exomeres (< 50 nm) to small (< 200 nm) and medium and large (> 200 nm) EVs. PalmGRET emits robust, sustained signals and allows the visualization, tracking and quantification of bionanoparticles from whole-animal to nanoscopic resolutions under different imaging modalities, including bioluminescence, BRET and fluorescence. Using PalmGRET, we show that EVs released by lung metastatic hepatocellular carcinoma (HCC) exhibit lung tropism with varying distributions to other major organs in immunocompetent mice. EV proteomics identified HCC-EV lung tropic protein candidates associated with cancer progression, in which SLCO2A1 and CLIC1 expression on non-tropic EVs conferred lung-tropism, while CD13 gave spleen tropism. Our results further demonstrate that redirected lung tropism decreases EV distribution to the liver, whereas the spleen tropism significantly reduces over time delivery to most major organs including the liver, kidneys, heart and brain. We anticipate our assays to be a starting point for more accurate and comprehensive *in vivo* models of EV biology and design. Furthermore, detailed *in vivo* EV characterization is critical for EV-based therapeutic developments, and a well-defined and quantitative assay for EV biodistribution profiles will be relevant for such development.

Introduction

Extracellular vesicles (EVs) are nanosized bioparticles (30–10,000 nm) released by cells to deliver bioactive cargoes to enable communications over short and long distances, both within and between organisms[1, 2]. Subtypes include exosomes (30–100 nm in diameter), shed microvesicles (or ectosomes, microparticles; 100–1,000 nm) and apoptotic bodies (50–4,000 nm)[3]. Using asymmetric flow field-flow fractionation (AF4), exosomes can be further subcategorized as small (Exo-S; 60–80 nm) or large (Exo-L; 90–120 nm) exosomes or bionanoparticle exomeres (< 50 nm)[4]. The EV subtypes (except exomeres) are lipid-bilayer encapsulated and released through two main pathways: i) fusion of the multivesicular bodies with the plasma membrane to release exosomes; or ii) outward budding and fission of the plasma membrane to release microvesicles. As EV subtype-specific isolation methods and terminology remain to be standardized[5], the generic term "EV" is used here unless otherwise specified.

To facilitate intercellular communication, EVs ferry bioactive cargoes between cells. These include DNA, RNA (*e.g.* mRNA, miRNA and lncRNA) and proteins (*e.g.* ligands and receptors), which have been associated with development, immune response, neurodegenerative diseases, developmental disorders and cancer progression[3, 6-10]. Tumour exosomes have been shown to be organotropic in facilitating subsequent metastasis to the tropic organs[11]. Specific integrins have been found to redirect tumour exosomes to the lungs (ITGβ_4) and liver (ITGβ_v). Concurrently, EVs are being actively explored as a diagnostic medium for liquid biopsy, in addition to serving as an endogenous delivery vehicle for therapeutic applications. Specifically, EVs have been designed with cell-type- and cancer-targeting moieties to enable the targeted delivery of therapeutic EVs[12]. However, the spatiotemporal dynamics of EVs *in vivo* remains elusive. For example, while organotropic and cell-targeting EVs may improve delivery to a particular site, their distribution to and relationship with other non-targeted tissues at organ systems level is largely unresolved. Moreover, accurate quantification of EVs has been confounded by a lack of suitable dyes and technical limitations[13, 14]. The biological understanding and therapeutic development of EVs would be greatly aided by the detailed characterization of EVs' spatiotemporal properties *in vivo*.

Conventional EV-labelling methods mainly rely on fluorescent (FL) dyes. Organic dyes such as PKH dyes, 1,1'-dioctadecyl-3,3,3'3'-tetramethylindocarbocyanine perchlorate (DiI) and its derivatives, or carboxyfluorescein succinimidyl ester (CFSE) have been widely-used in the study of EVs due to their stable and high FL signals[15, 16]. However, lipophilic FL dyes were later identified to spontaneously form nanometer sized micelles (*i.e.* false-positives) and carry an extended *in vivo* half-life (*e.g.* PKH2:

5–8 days, PKH26: > 100 days), resulting in inaccurate spatiotemporal detection of EVs[17, 18].

Bioluminescent (BLI) reporters have been used to label EVs for the *in vivo* imaging and pharmacokinetic analysis of administered EVs[19, 20]. However, the resolution is relatively poor when compared with that of FL dyes, and so conventional methods typically use BLI and FL reporters for *in vivo* and *in vitro* imaging, respectively. Bioluminescence resonance energy transfer (BRET) was developed to overcome some of these limitations[21]. Similar to the principle of fluorescence resonance energy transfer, BRET reporters are made of a pair of BLI and FL proteins conjugated in close proximity (30–70 Å) by a linker for intramolecular energy transfer. When treated with the substrate, BRET will emit both BLI and FL signals for detection. However, the use of BRET has been limited by BLI protein size, luminescence stability and intensity[22]. Nanoluc (Nluc) has recently overcome these obstacles to BRET; Nluc is a small (19 kDa), ATP-independent luciferase which provides one of the brightest glow-type bioluminescence for sustained excitation of the paired FL protein[22-25].

Previous studies have used EV markers fused to FL proteins (*e.g.* CD63-GFP) to examine EV distributions, but have mostly been limited to *in vitro* observations[26]. Meanwhile, multiphoton microscopy enables high resolution imaging of cells *in vivo* by exciting fluorophores with multiple photons at longer wavelengths for deeper tissue penetration (up to ~1 mm)[27]. However, it generally requires the imaging window to be fixed at one location to record cellular events longitudinally. We applied multiphoton microscopy to achieve *in vivo* visualization of EV release using pan-EV labelling FL EV reporters[28]. However, as EVs are circulated, they cannot be systemically tracked by multiphoton microscopy. Multiharmonic microscopy has also been applied successfully to imaging EVs *in vivo*, but it relies on the presence of specific metabolite signatures, and so is inapplicable to unspecified EVs[29, 30]. On the other hand, radioactive tracers such as ^{99m}Tc-HMPAO and ^{111}In-oxine have been applied to label EVs for *in vivo* imaging and EV biodistribution analysis using positron emission tomography–computed tomography (PET-CT) and single-photon emission computed tomography, respectively[31, 32]. However, the use of radioisotopes is limited to well-trained operators and certified facilities with available instruments, making these techniques costly and unsuitable for a general laboratory.

To overcome these limitations of EV visualization, we describe here a BRET-based EV reporter, PalmGRET, that enables multimodal, multi-resolution imaging and quantification of EVs from organismal to super-resolutions. PalmGRET was created by fusing a palmitoylation signal peptide sequence from growth-associated protein 43 (GAP43)[33] to the N-terminus of a GFP-Nluc BRET reporter (GpNluc)[22]. We

demonstrate that PalmGRET can label multiple bionanoparticle populations, including exomeres (< 50 nm) and small (< 200 nm; Exo-S) and medium and large (> 200 nm; Exo-L) EVs, making it a versatile reporter to visualize and monitor bionanoparticles released by cells. Moreover, PalmGRET specifically labels the EV inner membrane with a long-term and robust signal, thereby enabling live cell BLI and BRET microscopy, as well as super-resolution radial fluctuations (SRRF) nanoscopy[34] to observe EV dynamics *in vitro*. With its emitted BLI and BRET-FL signals, PalmGRET further allows *in vivo* imaging of administered EVs over an extended period of time (~20 min), as well as highly sensitive EV biodistribution analysis to detect minute EV changes in organs. Using PalmGRET, we identified lung-tropic EV proteins derived from lung metastatic hepatocellular carcinoma (HCA-1) in immunocompetent C3H mice, SLCO2A1 and CLIC1, which effectively redirected non-lung tropic human embryonic kidney 293T (293T) EVs to the lungs while reducing their distribution to the liver. In addition, CD13 (ANPEP, aminopeptidase N) was found to confer spleen tropism with a significantly decreased EV dissemination to multiple other organs including the liver, kidneys, heart and brain. Our results suggest that the *in vivo* function and therapeutic design of EVs should be considered at organ system level to account for their dynamic biodistribution.

Results

PalmGRET labels EVs at the inner membrane with FL and BLI reporter activities. To develop a multimodal and multi-resolution EV reporter, PalmGRET was created by genetically fusing the palmitoylation signal peptide sequence[35] of growth cone-associated protein 43 (GAP43)[33] to the N-terminus of a BRET pair, GpNluc[22] (**Fig. 1 a–c**). Upon stable expression in human 293T cells, PalmGRET uniformly labelled the plasma membrane to reveal an uneven membrane surface with bud-like structures at the apical plane and protrusions of the cells, which may be precursors to EV release (**Fig. 1d**). To examine whether PalmGRET can be applied to visualize EV release from multiple cellular populations, stable 293T-PalmGRET and 293T-PalmtdTomato cells[28] were co-cultured; both cell types were found to demonstrate EV release, thereby suggesting bidirectional EV-mediated intercellular communication (**Fig. 1e and Supplementary Movie 1**).

To characterize the EV labelling properties of PalmGRET, EVs isolated from stable 293T-PalmGRET and 293T-GRET cells (control) were examined by nanoparticle tracking analysis. The resulting EVs, EV-PalmGRET (147.7 ± 2.2 nm), EV-GRET (143.9 ± 3.8 nm; control) and EV-wildtype (EV-WT; 150.0 ± 3.5 nm; control), were all similar in size (**Fig. 2a, b**). Transmission electron microscopy with immunogold labelling further demonstrated that PalmGRET mostly localizes to EV

membranes (**Fig. 2c, d**). To mitigate possible steric hindrance to ligand–receptor interaction on the outer EV membrane[11, 36], we designed PalmGRET to label the inner EV membrane using the palmitoylation signal. To confirm the inner-membrane specificity of PalmGRET, we subjected the labelled EVs to dot blot analysis in the presence or absence of detergent (**Fig. 2e, f**). Whereas antibodies can only recognize proteins on the outer EV membrane in the absence of the detergent, the addition of TWEEN-20 (0.1% v/v) enables antibody entry and immunolabeling of proteins at the inner membrane by disrupting the EV membranes. Therefore, as EV-GRET showed a dim signal with the detergent and no signal in its absence, GRET appeared to be non-specifically packaged into the EV lumen (**Fig. 2e**). By contrast, a strong EV-PalmGRET signal was detected only in the presence of the detergent, thereby indicating inner membrane-specific labelling of EVs (**Fig. 2f**).

To verify the BLI function and EV-specificity of PalmGRET, isolated EVs were subjected to sucrose density gradient fractionation followed by BLI assay. In both the EV fractions (**Fig. 2g**) and pelleted EVs (**Fig. 2h**), EV-PalmGRET showed ~20 times the BLI activity of the EV-GRET control. Western blot analysis of the pelleted EVs further demonstrated that PalmGRET coincided with EV markers (CD63 and Alix)[37] at the EV-containing fractions (1.117–1.163 $g \cdot cm^{-3}$; **Fig. 2i** and **Supplementary Fig. 1**). Overall, PalmGRET efficiently and specifically labelled the inner EV membrane while functioning as a BLI reporter.

PalmGRET labels multiple bionanoparticle populations. An EV subtype-specific protein has yet been identified. In fact, multiple tetraspanins (CD63, CD81 and CD9) have been recommended to identify subpopulations of small EVs (sEVs)[38]. While studies have commonly focussed on a specific EV subpopulation to investigate its biological function, we envision multiple EV subtypes working simultaneously in mediating EV-based intercellular communication, especially *in vivo*. Therefore, we designed PalmGRET as a pan-EV labelling reporter to label and examine multiple bionanoparticle populations. Using AF4, Zhang *et al.* subcategorized small EVs (sEVs) as Exo-L (90–120 nm), Exo-S (60–80 nm), and non-membranous bionanoparticles exomeres (< 50 nm), each with different molecular profiles[4]. To further examine the pan-labelling coverage of bionanoparticles by PalmGRET, we performed AF4 on EV-PalmBRET and characterized fractions corresponding to Exo-L (P4), Exo-S (P3) and exomeres (P2) (**Fig. 3a**). To verify PalmGRET-labelling of the sEV fractions, the fractions (P2, P3 and P4) were subjected to BLI assay, which revealed ~10-fold stronger BLI and BRET-FL signals in PalmGRET-labelled Exo-L, Exo-S and exomeres when compared to that of GRET (**Fig. 3b, c**). While Exo-S and Exo-L of EV-PalmGRET exhibited no significant differences, exomeres showed

significantly lower signals in both BLI and BRET-FL activities, which positively correlates to the particle abundance of the three sEV subtypes as found by the quasi-elastic light scattering (QELS) detector (**Fig. 3a**). Interestingly, the PalmGRET-labelled exomere fraction showed a slightly increased hydrodynamic radius (~40 nm) than the GRET control (~35 nm), suggesting that PalmGRET slightly increases the size of exomeres while remaining under 50 nm in diameter. We further demonstrated that PalmGRET effectively labels Exo-S isolated from 0.22 μm-filtered conditioned media (**Fig. 2, 3d, e**), as well as Exo-L harvested from 0.8 and 1.2 μm-filtered media (**Supplementary Fig. 2**). We therefore confirmed that PalmGRET labels differently sized bionanoparticles ranging from exomeres to sEVs including Exo-L[5].

PalmGRET-labelled EVs exhibit robust and long-term BLI and BRET-FL signals. To characterize PalmGRET's BLI properties, EV-PalmGRET was supplemented with furimazine (Fz) substrate and measured for BLI and BRET-FL activities over time. EV-PalmGRET demonstrated a significantly higher signal in both the BLI and BRET-FL channels than either EV-GRET or EV-WT control (**Fig. 3d, e**). Interestingly, 293T-GRET cells emitted higher BLI and BRET-FL signals than 293T-PalmGRET cells (**Supplementary Fig. 3a, b**). EV-PalmGRET showed a similar BRET ratio to EV-GRET, indicating that the labelling of GRET to EVs using the palmitoylation moiety does not affect BRET efficiency (**Fig. 3f**). The BRET ratio of 293T-PalmGRET and 293T-GRET cells were also similar, further supporting that PalmGRET does not affect reporter function (**Supplementary Fig. 3c**). While EV-GRET exhibited approximately twice the BLI signal half-life of EV-PalmGRET (18.8 ± 0.99 min *vs.* 9.7 ± 3.67 min, respectively) and a significantly longer BRET-FL signal half-life (22.1 ± 0.41 *vs.* 15.0 ± 1.93 min, respectively), EV-PalmGRET displayed a distinctly higher signal over time (AUC, area under curve) than EV-GRET to enable robust signals and prolonged imaging of EVs (BLI: 15.0 ± 2.51 *vs.* 4.4 ± 0.90 RLU·min/particles, respectively; BRET-BLI: 22.0 ± 3.60 *vs.* 7.9 ± 1.89 RFU·min/particles, respectively) (**Fig. 3g, h**). In contrast, 293T-PalmGRET cells showed a longer half-life than 293T-GRET cells (BLI: 27.4 ± 1.30 *vs*. 21.3 ± 0.35 min, respectively; BRET-FL: 26.8 ± 1.4 *vs*. 19.7 ± 0.32 min, respectively) but lower AUCs (BLI: 20.7 ± 1.25 *vs.* 31.2 ± 0.66 RLU·min/particles, respectively; BRET-FL: 20 ± 1.30 *vs.* 28.2 ± 0.87 RLU·min/particles, respectively) (**Supplementary Fig. 3d, e**). The observed difference in PalmGRET activities between the labelled EVs and cells may be attributed to a variation in membrane-to-cytosol ratio: an EV particle has a higher membrane-to-cytosol ratio, while the opposite is the case for a cell[39]. In this way, PalmGRET locates to the plasma membrane and hence is more enriched per EV, whereas GRET predominately distributes to the cytosol and therefore is more

abundant per cell. Consequently, EV-PalmGRET showed stronger BLI and BRET-FL signals (and lower half-lives) as more Nluc enzyme is available to oxidize Fz when compared with EV-GRET, thereby yielding greater AUCs. Similarly, 293T-GRET cells generate higher AUCs with more abundant Nluc available per cell. Taken together, EV-PalmGRET emits strong and sustained signals for extended visualization and tracking of EVs.

PalmGRET enables multimodal and super-resolution imaging of cells and EVs. To examine PalmGRET imaging functions under microscopy, 293T-PalmGRET and 293T-GRET cells were examined for BRET-FL and FL signals under live-cell microscopy. We first confirmed BRET-FL activity by detecting the emitted GFP signal *via* BRET (BRET-FL) by bioluminescence microscopy following Fz substrate administration, where PalmGRET primarily locates to the membrane while GRET mostly accumulates at the cytosol (**Supplementary Fig. 4**). Epifluorescence microscopy was next applied to image the same samples, and a similar subcellular distribution pattern of PalmGRET and GRET was observed, thereby validating the observed BRET-FL signals (**Fig. 4a** and **Supplementary Fig. 4**). In addition, EVs could be visualized under epifluorescence microscopy only in 293T-PalmGRET and not 293T-GRET cells. To resolve EV signals at super-resolution, SRRF nanoscopy successfully resolved individual PalmGRET-EV signals (**Fig. 4a,** i–ii). We therefore employed SRRF nanoscopy in all subsequent subcellular EV imaging experiments, and readily visualized released EVs at super-resolution in real-time *in vitro* (**Fig. 4b, c** and **Supplementary Movies 2, 3**). We further tested the capability of PalmGRET in detecting EVs in fixed tissues, and successfully detected EV-PalmGRET signals inside cells of immunostained sections of EV-PalmGRET-injected mouse lung tissue (**Fig. 4d**). These results demonstrate PalmGRET's versatility in investigating cellular and subcellular distribution of EVs in live cells, as well as in preserved tissues.

Visualization, tracking and quantification of EV-PalmGRET from whole animal to nanoscopic resolutions. While our previous GlucB reporter allows *in vivo* imaging of EVs, the signal half-life is short (< 5 min) due to the flash-type emission of *Gaussia* luciferase[20, 40]. In addition to facilitating multi-resolution imaging, PalmGRET was designed to enable EV imaging for an extended period of time by employing Nluc, which has been reported to carry a BLI signal half-life > 2 h[41]. To examine *in vivo* imaging using PalmGRET, 100 μg PBS-washed EV-293T-PalmGRET was IV-injected to C3H mice followed by Fz administration to image the EVs *in vivo* (**Fig. 5a**). Of note, 1.2 μm-filtered conditioned media was used to harvest PalmGRET-EVs to observe the distribution dynamics of multiple EV subtypes *in vivo*. We

longitudinally tracked *in vivo* the EV distribution signal for up to ~20 min under three different imaging modes (BLI, BRET-FL and FL). Regions corresponding to the lungs and liver appeared to show the highest signals in the BLI and BRET-FL channels (**Fig. 5b**). To confirm this observation, major organs were harvested from EV-injected mice at 30 min and immersed in Fz solution for *ex vivo* imaging. The lungs showed the highest signal followed by the spleen and livers, whereas the brain, heart and kidneys exhibited negligible signals, corresponding to the EV signals detected *in vivo* (**Fig. 5c**). While both BLI and BRET-FL channels yielded clear and distinguishable EV signals, the FL channel resulted in a high and non-specific background under external excitation despite its shorter exposure time of 1 s (compared with 60 and 30 s for live animals and harvested organs, respectively, for BLI and BRET-FL).

We further visualized EV distributions in the lungs, spleen, liver and kidneys using nanoscopy. The EV-293T-PalmGRET-injected group showed a non-uniform and sporadic distribution of the EVs in the lungs (**Fig. 5d**). A similar distribution trend was also observed in the spleen, liver and kidneys, suggesting EV uptake by organs is tissue/cell-specific (**Supplementary Fig. 5**). This observation corroborates the findings of Hoshino *et al.* that EVs derived from malignant breast cancer cells are taken up by specific cell types including SPC^+ epithelial cells and $S100A4^+$ fibroblasts[16]. Quantification of EV signals from seventy SRRF images per organ with ImageJ[42] showed that the lungs contained the highest EV signals followed by the spleen, liver and kidneys (**Fig. 5e** and **Supplementary Fig. 5, 6**), hence corroborating the EV distribution pattern observed by *in vivo* and *ex vivo* imaging (**Fig 5b, c**). The same imaging and analysis parameters were applied to all tissue samples. Taken together, PalmGRET accurately revealed EV biodistributions with quantification at multiple levels of organization from whole animals and organs to tissues and cells.

Redirected organotropisms of EVs yield distinct biodistribution profiles. Tumour EVs have been reported to be tropic to pre-metastatic niches to promote subsequent tumour metastasis[11]. Other works have decorated EVs with cell type- and cancer-directing peptides such as rabies viral glycoprotein RVG and GE11, respectively, for targeted delivery of therapeutic EVs[43]. However, the spatiotemporal dynamics of EV biodistribution following redirection of EV tropism remains largely unknown. To explore this phenomenon, we applied the EV-PalmGRET system to elucidate the spatiotemporal properties of EV in the context of redirected EV tropism. We established the PalmGRET system in a mouse hepatocellular carcinoma cell line, HCA-1, which exhibits spontaneous lung metastasis in immunocompetent C3H mice[44], thereby generating stable HCA-1-PalmGRET cells. The lung metastatic potential of HCA-1-PalmGRET cells was confirmed by orthotopic implantation and

detection of tumour formation in both the liver and lungs (**Fig. 6 a, b**).

As tumour EVs have been shown to target pre-metastatic niches[11], we hypothesized that EVs released by HCA-1-PalmGRET will be lung tropic to promote subsequent metastasis. To examine this possibility, we educated immunocompetent C3H mice with 30 μg EV-HCA-1-PalmGRET (or EV-293T-PalmGRET as a control), and conducted BLI analysis to monitor EV biodistributions in the major organs (**Fig. 6c**). Remarkably, EV-HCA-1-PalmGRET showed a greater distribution to the lungs and liver (50.7% ± 5.40% and 18.3% ± 3.24%, respectively) when compared with EV-293T-PalmGRET (34.6% ± 0.22% and 5.8% ± 0.41%, respectively) at 0.5 h post-injection (**Fig. 6d**), indicating its immediate lung-tropic effect. After 72 h, the percentage EV-HCA-1-PalmGRET distribution in the lungs remained similar (54.7% ± 3.78%), thereby revealing sustained lung tropism. Interestingly, EV-293T-PalmGRET distribution significantly dropped from to 20.8% ± 0.35% in the lungs, but rose to 68.4% ± 2.81% ($p < 0.0001$) in the spleen from 0.5 to 72.5 h, suggesting that non-lung tropic EVs were distributed to the highly vascularized spleen as a transitory reservoir (**Supplementary Table 3**; 0.5 vs 72.5 h). The kidneys, heart and brain showed lower percentages of EV distribution (< 10%) for both EVs. The EV biodistribution pie charts for the major organs show a distinct pattern in which EV-HCA-1-PalmGRET mainly distributed to the lungs, livers and spleen, whereas EV-293T-PalmGRET mostly located to the spleen followed by the lungs (**Supplementary Fig. 7**). Note that 30 μg EV-HCA-1-PalmGRET was administered every 24 h based on the finding that this amount yielded minimal signals in the blood circulation 30 min post-injection, suggesting that the majority of the EVs had been distributed to the organs while leaving a minimal amount in the circulation (**Supplementary Fig. 8a**). While most of the EV signals were detected in the EV-enriched qEVoriginal fraction (F8) from the plasma, the neighbouring fractions (F7 and F9) showed lower EV signals, demonstrating the EV-specificity of PalmGRET (**Supplementary Fig. 8b**). As C3H mice are immunocompetent, we also performed multiplex cytokine tests on mice serum, and confirmed that the EV injections did not induce an acute immune response, which may have led to a biased uptake in the lungs, livers or spleen (**Supplementary Table. 4**)[45].

Given that EV-HCA-1-PalmGRET exhibited lung tropism and a different biodistribution profile from that of EV-293T-PalmGRET, we set to redirect EV-293T-PalmGRET to the lungs to investigate the subsequent EV distribution dynamics to non-targeted organs. We identified several lung tropic protein candidates by proteomic analysis of EV-HCA-1-PalmGRET. Among the 521 detected proteins (**Supplementary Table. 5**), we selected four candidates by screening for lung tropism-related membrane proteins using Uniprot[46] followed by association to HCC

progression, lung metastasis and lung cancer progression: CD13[47], CLIC1[48], SLCO2A1[49] and NHERF1[50].

Following overexpression of the proteins in non-lung tropic 293T-PalmGRET cells and hence decoration of the derived EVs (**Supplementary Fig. 9**), we harvested and administered the EVs at 10 μg per 24 h for 72 h to investigate the redirected lung tropism and biodistribution in C3H mice (**Fig. 6e**). At 0.5 h post-injection, the SLCO2A1 group showed an elevated percentage of EVs in the lungs compared with the WT control (**Fig. 6f**). The CLIC1 group showed a similar increase, albeit not statistically significant. At 72.5 h, both SLCO2A1 and CLIC1 groups showed a significant redirection of the EVs to the lungs when compared with the WT control, suggesting that repeated exposure to lung-tropic EVs augments the tropic effect over time (**Supplementary Table 6**). The two groups also demonstrated a decline in EV distribution in the livers, suggesting the redirected lung tropism shifts EV distribution away from the liver and to the lungs (**Fig. 6f** and **Supplementary Fig. 10**). A high mRNA level and moderate-high expression of SLCO2A1 have previously been identified in primary and metastatic liver cancers[49], and SLCO2A1 upregulation has been reported to promote lung cancer invasion using a PI3K/AKT/mTOR pathway[51]. Similarly, downregulation of CLIC1 has been shown to decrease the invasion and migration of HCC cells[52], whereas overexpression in HCC was found to correlate to larger tumour size, distal metastasis, aggressive pathologic tumour phenotype, nodes and poor survival rate[53]. On the other hand, the CD13 group yielded spleen tropism with a high percentage of EV distributed to the spleen and a significant decrease in other major organs (*e.g.* liver, kidney, heart and brain, but not the lungs). Dendritic cells in the red pulp and interdigitating cells in the white pulp of the spleen express CD13[54], which is responsible for immune cell trafficking and adhesion to endothelial cells[55]. Therefore, the redirected tropisms by SLCO2A1, CLIC1 and CD13 overexpression on EV-293T-PalmBRET concur with their respective biological functions. The NHERF1 group yielded neither lung tropism nor an altered biodistribution profile when compared with the WT control. As NHERF1 is endogenously expressed in 293T-PalmGRET cells and EVs, its overexpression does not readily affect its native EV biodistribution profile (**Supplementary Fig. 9a**). Additional investigation will be required to elucidate the specific tissues and cells facilitating EV uptake by each organ. In summary, we demonstrate that while redirected EV tropism enhances delivery to a targeted organ, its distribution to other major organs will also be dynamically altered, possibly yielding a different function at organ systems level.

Conclusions

Accurate visualization and tracking of EV distribution are critical in understanding the role of EV-mediated cell-to-cell communication in diseases and therapy. Here we established a multimodal and multi-resolution PalmBRET method to enable pan-bionanoparticle labelling and imaging and therefore quantification in live cells, whole animals, and preserved tissues. The method can resolve the intricate spatiotemporal dynamics of EVs. PalmGRET revealed that EVs derived from lung metastatic HCC are lung tropic, and the tropism can be conferred to non-lung-tropic EV-293T by decorating EVs with identified HCC-EV membrane proteins. Importantly, the enhanced EV delivery to tropic organs also significantly alters its distribution to other major organs. Our findings suggest that the dynamics of EV biodistribution and targeted design should be investigated at organ systems level in EV biology and therapeutic developments, respectively **(Fig. 7)**.

Methods

Cell culture. Human embryonic kidney 293T (HEK293T) cells (a gift from Dr. Chen-Wen Jeff Chan, National Tsing-Hua University) and mouse hepatocellular carcinoma cells from C3H strain HCA-1 (a gift from Dan Duda, Massachusetts General Hospital) were maintained in DMEM (high glucose [4,500 mg/L], Hyclone, South Logan, Utah, USA) supplemented with 10% fetal bovine serum (Hyclone), penicillin (100 U/mL) and streptomycin (100 μg/mL) (Hyclone). For stable HEK293T-GRET/PalmGRET cell line maintenance, 1 μg/mL of puromycin (MDbio, Taipei, Taiwan) was added to the culturing medium. Stable HCA1-PalmGRET cells were stored in early passages, and maintained in the culturing medium without puromycin, which was found to affect cellular phenotype. All culturing media were supplemented with plasmocin (2.5 μg/mL; Invivogen, San Diego, California, USA) to mitigate mycoplasma contamination. Both puromycin and plasmocin were removed for two cell passages prior to subsequent experiments.

Animal studies. C3H/HeNCrNarl male mice were purchased from BioLASCO Taiwan Co., Ltd. (Ilan, Taiwan) for all implantation, EV injection, and EV-tropism studies. For euthanasia, 200 μL Zoletil 50 (25 mg/mL) and xylazine (20 mg/mL) were intramuscularly injected into mice thigh followed by cervical relocation. All animals received humane care in compliance with the Guide for the Care and Use of Laboratory Animals published by the National Academy of Sciences, and all study procedures and protocols were approved by the Animal Research Committee of National Tsinghua University (Hsinchu, Taiwan).

Molecular cloning. All primers are listed in **Supplementary Table 1**. pENTR-

backbone was created by treating pENTR-Luc (w158-1, a gift from Drs. Eric Campeau and Paul Kaufman; Addgene plasmid #17473) with NcoI and XbaI (New England Biolabs, Massachusetts, USA) followed by gel purification. GRET and PalmGRET fragments were PCR amplified with Q5® High-Fidelity DNA polymerase (New England Biolabs) from pRetroX-Tight-MCS_PGK-GRETNLuc (a gift from Antonio Amelio; Addgene plasmid #70185)[22]. GRET fragment was flanked by two restriction enzyme sites, NcoI and XbaI at the 5' and 3' ends, respectively. The NcoI-GRET-XbaI fragment was then enzyme digested by Nco I and Xba I, gel purified and ligated with pENTR (w158-1)-backbone by Quick Ligation kit (New England Biolabs) to create pENTR-GRET. Palmitoylation signal sequence was added to 5' end of the GRET fragment through primer synthesis to generate PalmGRET fragment. pENTR-PalmGRET was then constructed *via* NEBuilder HiFi DNA Assembly (New England Biolabs) to insert PalmGRET fragment into the pENTR-backbone. pLenti DEST CMV Puro-GRET/PalmGRET plasmids were created by Gateway LR cloning with pENTR-GRET/PalmGRET and pLenti DEST CMV Puro plasmids (a gift from Drs. Eric Campeau and Paul Kaufman; Addgene plasmid #17452)[56] using LR Clonase II Plus (Invitrogen, Carlsbad, California, USA).

Lentivirus production. For GRET and PalmGRET lentivirus productions, a protocol from *Addgene.org* was used. Briefly, the culture medium of 70-80% confluent HEK293T cells in a 10 cm cell culture dish was replaced with 10 ml DMEM supplemented with GlutaMAX™ (Gibco, Massachusattes, USA), 10% FBS (Hyclone) and 25 µM chloroquine diphosphate (Tokyo Chemical Industry, Tokyo, Japan) at 5 h prior to transfection. 293T cells were co-transfected with 1.3 pmol psPAX2 (a gift from Didier Trono; Addgene plasmid # 12260), 0.72 pmol pMD2.G (a gift from Didier Trono; Addgene plasmid # 12259), and 1.64 pmol pLenti DEST CMV Puro-GRET- or -PalmGRET by PEI transfection (polyethylenimine, linear, MW 25,000, Alfa Aesar, Massachusetts, USA; 1 mg/ mL). The ratio of DNA:PEI was 1:3 diluted in 1 ml of OptiMEM (Gibco). At 18 h post-transfection, the viral medium was replaced with virus production medium (15 ml DMEM supplemented with GlutaMAX and 10% FBS). At 48 h post-transfection, the viral medium was harvested, stored at 4°C and replaced with 15 ml virus production medium. At 72 h post-transfection, the virus-containing media were pooled and centrifuged at 500 x *g* for 10 min at 4°C. The viral supernatant was filtered through a 0.45 µm PES filter (Pall, New York, USA), aliquoted into 1.5 mL microcentrifuge tubes, snap frozen by liquid nitrogen, and stored at -80°C.

Generation of stable cell lines. To generate stable 293T-GRET/PalmGRET and

HCA1-GRET/PalmGRET cells, 5 x 10^4 293T or HCA-1 cells were resuspended in 1 mL DMEM supplemented with GlutaMAX^{TM} (862 mg/L of L-Alanyl-Glutamine), 10% FBS and 10 µg/ml polybrene (Sigma-Aldrich, Missouri, USA), added to 6-well plates containing GRET/PalmGRET lentivirus, and cultured at 37 °C with 5% CO_2 in a humidified incubator. At 72 h post-transduction, transduced HCA-1 cells were sequentially expanded to 6, 10 and 15 cm dishes for fluorescence-activated cell sorting (FACS) to harvest GFP-positive HCA-1 cells. Transduced HEK293T cells were selected by 1 µg/ mL of puromycin.

EV isolation. Stable 293T-GRET/-PalmGRET and HCA1-PalmGRET cells (4.5 x 10^6 of 293T stable cells or 2.5 x 10^6 of HCA-1-PalmGRET) were cultured in DMEM high glucose supplemented with 5% EV-depleted FBS, penicillin (100 U/mL) and streptomycin (100 µg/mL) for 48 h at 37 °C with 5% CO_2 in a humidified incubator. Conditioned medium (CM) from cell culture dishes with 80-90% cell confluency were pooled and subjected to differential centrifugation. CM was sequentially centrifuged at 300 *x g* and 2,000 x *g* at 4 °C for 10 minutes to remove cells and cell debris, respectively. CM was then filtered through a 0.22 (for characterization studies), 0.8 (for characterization studies) or 1.2 µm (for characterization studies and tropism studies) pore size PES filter (Pall) and centrifuged at 100,000 *x g* at 4 °C for 90 minutes to collect EV pellets in double 0.22 µm-filtered PBS.

For tropism study and time-lapse *in vivo* imaging, the harvested EVs were resuspended with 3 mL double 0.22 µm-filtered PBS and centrifuged under 100,000 *x g* at 4 °C for 70 mins to remove non-EV contaminants. The washed EVs were resuspended in double filtered PBS, and protein concentration was determined by Pierce BCA Kit (Thermo Scientific, Massachusetts, USA). EV samples were aliquoted and stored at -80 °C to maintain same freeze and thaw cycle.

For EV blood clearance study, 30 µg of EV-HCA-1-PalmGRET were IV-injected into C3H mice *via* the tail vein. At 0, 5, 30, and 60 min post-injection, the mice were anesthetized by intramuscular injection of 200 µL Zoletil 50 (25 mg/mL) and xylazine (20 mg/mL) cocktail, and blood samples was collected through cardiac puncture. Syringe and sterilized 1.5 mL microcentrifuge tube (Biomate, Taiwan) were pre-rinse by 0.5 M, pH 8 ethylenediaminetetraacetic acid (EDTA, Invitrogen) to prevent blood coagulation. 500-700 µL of mice whole blood was centrifuged at 1,500 *x g* for 10 min at 4 □, and the supernatant was transferred to a new 1.5 mL microcentrifuge tube for additional centrifugation at 2,000 *x g* for 15 min at 4 °C. The isolated plasma samples were stored at -80 °C prior to EV isolation. For EV isolation from mice plasma, less than 500 µL of mice plasma was loaded into qEVOriginal 70nm columns (iZON Science, Christchurch, New Zealand) based on the

manufacturer's instruction. Double 0.22 µm-filtered PBS was used as the running phase. Fractions 7-9 were individually collected (500 µL/fraction) and concentrated by Amicon Ultra-0.5 centrifugal filter unit with 10 kDa membrane (Merck Millipore) with 14,000 *x g* at 4 °C for 8 min centrifugation to have final volume less than 100 µL. Final volume of the concentrates was recorded for data analysis.

Nanoparticle tracking analysis. NanoSight NS300 (Malvern Panalytical, United Kingdom) was used to determine the size and particle concentration of isolated EVs. NTA Version: NTA 3.2 Dev Build 3.2.16. Triplicate sample measurements using capture camera level: 14 with temperature control of 25 °C ± 0.01.

Transmission Electron Microscopy and Immunogold Staining. Isolated EVs were pelleted at 20,000 x *g* for 30 min at 4 □ followed by fixation with 4% formaldehyde in PBS for 2 h. Fixed EVs were cryosectioned and immunolabeled with anti-GFP (rabbit; ab6556, Abcam, Cambridge, UK) and anti-CD63 (mouse; 556019, BD Pharmingen, San Diego, USA) followed by rabbit anti-mouse conjugated with 5 nm gold-labeled secondary antibodies (University Medical Center, Utrecht, The Netherlands). Images were captured using Tecnai G^2 Spirit Bio TWIN transmission electron microscope.

Sucrose density gradient analysis. For sucrose gradient fractionation, 8, 30, 45, 60 % (w/v) sucrose (J.T.Baker, Pennsylvania, USA) in PBS, pH 7.4 were layered, and isolated EVs were loaded on top of the discontinuous sucrose gradient followed by centrifugation at 268,000 x *g*, 4 °C for 38 min with MLA-50 rotor (Beckman Coulter, California, USA). The top layer and the subsequent 10 fractions (fraction 1-10) were collected. 16.5 µL of each fraction was saved for BLI activity assay. To pellet EVs, fractions 2-9 were diluted 1:10 in PBS and centrifuged at 100,000 x *g*, 4°C for 1 h with MLS-55 rotor (Beckman Coulter). The pellets were lysed in 40 µL of radioimmunoprecipitation (RIPA) buffer supplemented with protease inhibitor cOmplete protease inhibitor cocktail (Roche, Basel, Switzerland). 6.6 µL of each pelleted fraction was saved for BLI activity assay.

Western blot analysis. Cells and EVs were lysed in RIPA lysis buffer (1X PBS, pH 7.4, with 1% Igepal CA-630, 0.5% sodium deoxycholate, 0.1% SDS) with cOmplete protease inhibitor cocktail (Roche). Protein concentrations of EVs and cell lysates were determined using Pierce™ BCA Protein Assay Kit (Thermo Scientific). Protein lysates were separated using Bolt™ 4-12% Bis-Tris Plus Gels (Invitrogen) and transferred onto 0.2 µm nitrocellulose membranes (Amersham Bioscience, Little

Chalfont, UK). The membranes were blocked with 5% BSA (Cyrusbioscience, Taiwan) in PBST (1X PBS, pH 7.4, with 0.1% Tween-20) for 1 h at room temperature and immunoprobed with primary antibodies overnight at 4 °C. The membranes were washed three times in PBST at room temperature, incubated with secondary antibodies for 1 h at room temperature followed by another three washes in PBST. For Western blots of purified EV pellets from sucrose gradients, the membranes probed by HRP-conjugated secondary antibodies were developed by chemiluminescence using Trident Femto Western HRP Substrate kit (GeneTex) with MultiGel-21 Imaging System (Topbio, Taiwan). For Western blots of EV overexpression experiment, the overexpressed proteins and GAPDH immunoprobed by IR-dye-conjugated secondary antibodies were imaged by ODYSSEY CLx (LI-COR Biosciences, Nebraska, USA). GAPDH for SLCO2A1 overexpressed group, as well as ALIX immunoprobed by goat anti-mouse HRP-conjugated secondary antibody were developed by chemiluminescence using Trident Femto Western HRP Substrate kit (GeneTex) and imaged with MultiGel-21 Imaging System (Topbio). Antibody dilutions and hosts are provided in **Supplementary Table 2**.

Dot blot analysis. To characterize membrane orientation of PalmGRET and GRET in EVs, EVs isolated from 0.22 μm-filtered CM were serially diluted to the following concentrations: 31.25 ng, 62.5 ng, 125 ng, 250 ng, 500 ng, 1,000 ng, 2,000 ng in 5 μL. Cell lysates were diluted to 2,000 ng in 5 μL as positive controls. 5 μL of diluted EVs, cell lysates, and double-filtered PBS were dotted onto 0.45 μm nitrocellulose membranes (Amersham Bioscience) and blocked in 10% BSA supplemented PBS overnight at 4 °C. The membranes were immunoprobed with anti-GFP antibody (GeneTex) diluted in 5% BSA in PBS or PBST overnight at 4 °C, wash three times in PBS or PBST for 30 minute each, and incubated with HRP-conjugated secondary antibodies for 1 h at room temperature followed by another 3 washes. The membranes were developed by chemiluminescence using ECL Select™ Western Blotting Detection Reagent (Amersham Bioscience) and MultiGel-21 Imaging System (Topbio). Antibody dilutions and hosts are provided in **Supplementary Table 2**.

Asymmetric-flow field-flow fractionation (AF4). AF4 of EV-GRET/-PalmGRET was performed based on the protocol described by Zhang and Lyden [57] with minor modifications. Briefly, 4.5 x 10^6 293T-PalmGRET or -GRET cells were seeded in 15 cm culture dishes (Thermo Scientific) with DMEM high glucose (Hyclone) supplemented with 5% EV-depleted FBS, penicillin (100 U/mL, Hyclone) and streptomycin (100 μg/mL, Hyclone) for 48 h at 37 °C with 5% CO_2 in a humidified incubator. After 48 h, CM were pooled into 50 mL centrifuge tubes (Biomate) and

605 centrifuged at 500 *x g* for 10 min, 10°C followed by 12,000 *x g* for 20 min, 10°C. CM
606 were then centrifuged at 100,000 *x g* for 90 minutes, 4 °C with 70Ti rotor (Beckman
607 Coulter) to collect EV pellets in double 0.22 µm-filtered PBS. The harvested EVs
608 were resuspended with 3 mL double filtered PBS and centrifuged with MLA-55 rotor
609 (Beckman Coulter) under 100,000 *x g* at 4 °C for 70 mins to remove non-EV
610 contaminants. The washed samples were resuspended in double filtered PBS, and
611 protein concentration was determined by Pierce BCA Kit (Thermo Scientific). EV
612 samples were adjusted to 0.5 mg/mL and stored at -80 °C. Before loading to AF4, the
613 frozen EV-GRET and -PalmGRET were thawed on ice and centrifuged at 13,000 x g
614 at 4°C for 5 min. 100 µL of the supernatant was injected to AF4 (Eclipse DualTec;
615 Wyatt, California, USA) to collect the EV subpopulations. The same AF4 parameters
616 were set as described in Zhang ***et al.***[57]. Resulting fractions were collected in 1 mL
617 deep 96-well plate (Greiner Bio-One, Germany) for 500 µL/well. P2, P3 and P4
618 comprise of fractions from 13.5 min to 19 min, 22 min to 27 min, and 31 min to 34.5
619 min, respectively. The pooled fractions were transferred to ice-cold PBS pre-rinsed
620 Amicon Ultra-4 centrifugal filter units with Ultracel-30 membrane (Merck Millipore,
621 Massachusetts, USA), then centrifuged with 3,200 *x g* at 4 °C for 10 min. The
622 centrifugation was repeated until the concentrate volume was less than 100 µL. The
623 final volume of each population was recorded for data analysis.
624
625 **Live-cell imaging.** To setup live-cell fluorescent imaging, 1 x 10^4 293T-GRET/-
626 PalmGRET cells were seeded per well into a glass-bottom 8-well chamber (#1.5,
627 Nunc™ Lab-Tek™ II Chamber Slide™ System, Thermo Scientific) coated with poly-
628 D-lysine (Mw 75,000-150,000 Da, Sigma-Aldrich), and incubated overnight in 250
629 µL DMEM high glucose without phenol red (Hyclone) supplemented with 10% FBS
630 (Hyclone), penicillin (100 units/ml, HyClone) and streptomycin (100 µg/ml,
631 HyClone). Cells were then imaged at 37 °C in a chamber supplemented with
632 humidified 5% CO_2 through 63x oil lens (NA= 1.4) with optovar set to 1.6x using
633 Axio Observer 7 epifluorescent microscope (Zeiss, Oberkochen, Germany) and
634 recorded by iXon Life 888 BV EMCCD (Andor Technology, Northern Ireland, UK).
635 Micro-Manager [58] was used to acquire the images with or without SRRF [34], and all
636 images were taken with the same parameter for DIC, GFP (epi-FL), or GFP (BRET),
637 or GFP (SRRF-FL). Images of GFP *via* BRET were acquired after adding furimazine
638 (Promega, Wisconsin, USA) diluted in culturing medium without phenol red (final
639 dilution: 1/500) into an 8-well chamber containing either 293T-GRET/PalmGRET
640 cells, then imaged by applying 530/50 nm emission filter without excitation light. To
641 setup live-cell confocal imaging for Z-stack reconstruction, 3 x 10^4 293T-PalmGRET
642 or 1.5 x 10^4 for both 293T-PalmGRET and 293T-PalmtdTomato cells were seeded into

35 mm glass-bottom (#1.5) dish (ibidi, Gräfelfing, Germany) coated with poly-D-lysine (Mw 75,000-150,000 Da, Sigma-Aldrich) and incubated overnight in 1.5 mL DMEM high glucose (Hyclone) supplemented with 10% fetal bovine serum (Hyclone), penicillin (100 units/ml, HyClone) and streptomycin (100 µg/ml, HyClone). Cells were then imaged at 37°C in a chamber supplemented with humidified 5% CO_2 through white light laser confocal microscope TCS SP8 (Leica, Wetzlar, Germany). **Supplementary Movie 1** was processed by Bitplane-Imaris 9.5 (Andor Technology) from images of **Fig. 1e** and **Supplementary Movie 2 and 3** were processed by Fiji (ImageJ, NIH).

HCA1-PalmGRET orthotopic implantation in C3H mice. C3H mice (Biolasco) were anesthetized, and 1 x 10^6 cells of HCA1-PalmGRET were mixed with 10 µL Matrigel (Corning, New York, USA) then orthotopically injected to the liver of 5-6 weeks old C3H mice as previous described[44].

Proteomics analysis and data processing. The sample were resolved in 10 mM tris (2-carboxyethyl) phosphine (Sigma-Aldrich) with 50 mM ammonium bicarbonate (Sigma-Aldrich) for 30 min at 37 °C and alkylated in 50 mM iodoacetamide (Sigma-Aldrich) with 50 mM ammonium bicarbonate for 45 min in the dark at 25°C. Trypsin/Lys-C (Promega) solution was added and incubated at 37 °C for 12 h. The resulting peptides were extracted from gel fragments and analyzed with Orbitrap Fusion Lumos Mass Spectrometer (Thermo Scientific) combined with UltiMate 3000 RSLC nano-flow HPLC system (Thermo Scientific) with HCD or EThcD MS/MS mode. Raw file of MS/MS spectra were processed for peak detection by using MaxQuant software version 1.6.5.01.[59] Peptide identification was performed by using the Andromeda search engine[60] and the Swiss-Prot database. EV-HCA-1-PalmGRET and EV-293T-PalmGRET were searched against UniProt Mus Musculus Database (Swiss-prot, 17,009 reviewed protein sequence, UP000000589) and Homo Sapien Database (Swiss-prot 26,445 reviewed protein sequence, UP000005640). Search criteria used in this study were trypsin specificity, fixed modification of carbamidomethyl, variable modifications of oxidation and acetyl (Protein N-term), and allowed up to 2 missed cleavages. A minimum of 5 amino acids in the peptide length was required. The precursor mass tolerance was 20 ppm, and the fragment ion tolerance was 0.5 Da. False discovery rate of 0.01 and Peptide Rank of 1 were set for peptide identification filters.

EV-tropism study. 30 µg of EV-PalmGRET or EV-HCA-1-PalmGRET was IV-injected to C3H mouse *via* the tail vein at 0, 24, 48, and 72 h. At 0.5 and 72.5 h post-

EV administration, each mouse was anesthetized and euthanized with cervical dislocation, and major organs including the brain, lungs, heart, livers, spleen, and kidneys were harvested for biodistribution analysis by bioluminescence assay. To study redirected EV tropism, pcDNA3.1 encoding human SLCO2A1, NHERF1, CLIC1, CD13 from total gene synthesis (GenScript, New Jersey, USA), or mock (PEI only) were transfected into 293T-PalmGRET cells with *via* PEI transfection in 15 cm dishes. At 24 h post-transfection, 4.5 x 10^6 transfected cells per dish were transferred to 4 x 15 cm culture dishes with DMEM high glucose (Hyclone) supplemented with 5% EV-depleted FBS (Hyclone), penicillin (100 U/mL, Hyclone) and streptomycin (100 µg/mL, Hyclone) for 48 h at 37 °C with 5% CO_2 in a humidified incubator followed by EV isolation. Timelines for EV administration and organ harvest are described in **Fig. 6**.

Immunohistochemistry. The kidneys, livers, lungs, and spleen were embedded in Tissue-Tek (OCT compound) and kept frozen at −80 °C. Tissues were sectioned (5 µm thickness), fixed in acetone at −20 °C for 10 min and washed with PBS. The sections were blocked with 5% BSA for 1 h at room temperature and incubated with primary antibodies at 4 °C overnight. Sections were washed with PBS and incubated with secondary antibodies for 1 h at room temperature. Sections were next washed by PBS and mounted using Prolong Diamond antifade mounting solution containing DAPI (Invitrogen). Primary and secondary antibody dilution for different organ tissues are listed in **Supplementary Table 2.** All sections were imaged using Axio Observer 7 epifluorescent microscope (Zeiss) equipped with iXon Life 888 BV EMCCD (Andor Technology) with or without SRRF with the same imaging parameters. Images (n = 70 per organ) were subjected to Fiji (ImageJ, NIH) for EV quantitative analysis with the same threshold. 5 x 5 tiled images were selected from 6 x 6 tiled images to remove uneven edges following tiling by Fiji (NIH).

Bioluminescence assays. GloMax® Discover Microplate Reader (Promega) with auto-injectors was set for Nluc (450/10 nm) and BRET-FL (510/10 nm) readings, and BRET ratio was calculated by dividing the acceptor signal (510/10 nm) with the donor signal (450/10 nm). To assess EV BL, 5 µL of crude EVs (triplicates), 5 µL of each fraction (triplicates), or 3 µL of pelleted fraction 2-9 (duplicates) were added into a 96-well white plate (Greiner Bio-One, Germany). Furimazine (Promega) was diluted 1:100 in PBS and 50 µL was added to each well by the auto-injector to detect Nluc and BRET signals with 0.5 sec integration time. To assess AF4 samples, 20 µL concentrates of P2, P3, and P4 of EV-293T-GRET/PalmGRET (triplicates) were added into a 96-well white plate (Greiner Bio-One). Furimazine (Promega) was

diluted 1:400 in PBS and 80 µL was injected into each well by the auto-injector to detect Nluc and BRET-FL signals with 1 sec integration time. To track time-lapse EV-PalmGRET/GRET signal, isolated EVs were re-suspended in double-filtered PBS and 5 µL of EVs were added per well (triplicates) into a 96-well white plate (Greiner Bio-One). Furimazine (Promega) was diluted 1:500 in PBS, and 45 µL of Fz solution was injected into EV-293T-GRET/PalmGRET *via* the auto-injector. BL and BRET-FL signals were measured every 5 minutes for a total of 4 h with 0.5 sec integration time. The collected signals were normalized to the number of cells or EV particles determined by a cell counter (Countess II^{TM}, Invitrogen) or NTA analysis, respectively.

For EV biodistribution analysis, the harvested organs were lysed by T-PER (0.5 g organ/mL T-PER, Thermo Scientific) with 1X Halt protease inhibitor (Thermo Scientific). Lysates were centrifuged at 10,000 *x g*, 4°C for 10 minutes followed by supernatant collection to acquire protein extracts from tissues. The supernatants were added to 96-well white plate (Greiner Bio-One) with 20 µL per well in triplicates. 80 µL of furimazine (Promega) with 1/400 dilution in PBS was auto-injected per well to have final dilution of 1/500. Integration time was set to 1 s for BLI readings.

To monitor time-lapse PalmGRET/GRET signals of live cells, 1 x 10^4 293T-PalmGRET, -GRET, and -WT cells were seeded per well in triplicates in a 96-well white plate coated with poly-D-lysine (Mw 75,000-150,000 Da, Sigma-Aldrich), and incubated overnight in 100 µL DMEM high glucose without phenol red (Hyclone) supplemented with 10% fetal bovine serum (Hyclone), penicillin (100 units/ml, HyClone) and streptomycin (100 µg/ml, HyClone). 50 µL culture medium was next removed from each well, and 50 µL furimazine (Promega) diluted 1:250 in the culturing medium was auto-injected into each well for detection of bioluminescent and BRET signals every 5 minutes for a total of 8 h with 0.5 sec integration time.

To measure plasma-derived EVs, 20 µL concentrates of fraction 7-9 from mice plasma (by qEV columns) were add into a 96-well white plate in triplicates (Greiner Bio-One). Furimazine (Promega) was diluted 1:400 in PBS, and 80 µL was injected into each well by an auto-injector to detect Nluc and BRET-FL signals with 1 sec integration time.

***In vivo* and *ex vivo* imaging.** To image biodistribution of administered EVs *in vivo*, 100 µg of EV-293T-PalmGRET (PBS washed) was IV-injected to C3H mouse *via* the tail vein at 0 min. The mice were anesthetized at 3 mins post-EV injection. At 5 mins post-EV injection, 1/40 diluted furimazine (Promega) in sterile 100 µL PBS was IV-injected to C3H mice *via* tail vein for IVIS imaging. Images were taken at 5, 10, 20, and 30 min post-Fz administration. Nluc and BRET-FL signal were acquired by applying open filter (no filter) and 500/20 nm, respectively. For epifluorescence signal,

excitation filter (470/30 nm) and emission filter (520/20 nm) were used. 60 and 30 sec exposure time were set for *in vivo* and *ex vivo* images, respectively; and 1 sec was set for externally excited fluorescence images to avoid overexposed images.

Prior to monitoring tumour progression, HCA1-PalmGRET bearing C3H mice were anesthetized. To acquire Nluc and BRET-FL signals, 1/40 diluted furimazine (Promega) in 100 μL sterile PBS was injected via the tail vein, and each mouse was imaged by applying open (for Nluc) and 500/20 nm (for BRET-FL) emission filters with 60 sec exposure time. Following live animal imaging, each mouse was anesthetized again, and euthanized with cervical dislocation. Major organs including the brain, lungs, heart, livers (with tumor), spleen, kidneys, intestine and colon were harvested for *ex vivo* imaging. The harvested organs were immersed in either 1/400 diluted furimazine (Promega) in sterilized PBS to detect Nluc/BRET-FL signal. The same filter settings were applied to collect Nluc and BRET-FL with 1 sec exposure time to avoid saturated signals.

Multiplex cytokine assay of mouse serum. Mice were anesthetized and the blood was collected by cardiac puncture at 0.5, 24.5, 48.5 and 72.5 h post-EV-HCA-1/-293T-PalmGRET injection. The blood of mice without EV injection were included as the baseline (control). 500-700 μL of mice whole blood were collected in 1.5 mL and allowed to clot at 4 °C for 30 min before centrifugation. After centrifugation with 1,500 *x g* at 4 °C for 10 min, the serum were transferred to a new 1.5 mL microcentrifuge and stored at -80 °C before Multiplex Cytokine Assay. Bio-Plex® Multiplex Immunoassays Assay (Bio-Rad, California, USA) was performed according to manufacturer's instruction. 50 μL serum was loaded per well into 96-well microplate, and each sample was test in duplicates. Murine IL-1β, IL-2, IL-4, IL-5, IL-6, IL-10, IL-12, IL-13, IL-17A, IL-22, IL-23, TNF-α, and IFN-γ signal were test by the Bio-Plex array reader (Bio-Rad).

Statistical analyses. Statistical analyses were performed using GraphPad Prism Version 7.05. Two-tailed Student's t-test was used for comparison between two groups. Two-way analysis of variance (ANOVA) followed by Tukey *post hoc* test, or ordinary ANOVA followed by Tukey or Dunnett *post hoc* test was used for comparison of three or more groups. Values were normally distributed, and the variance was similar between compared groups. Error bars for all the graphs represent mean ± SEM. P-value < 0.05 was considered statistically significant.

Acknowledgements

We thank to Dr. Wei Chun Huang from Biophysics Core Facility of Institute of

Atomic and Molecular Sciences for confocal laser microscopy imaging. We are grateful to Chia Chen Tai and Tzu Wen Tai from Flow Cytometry Core Facility under Academia Sinica Core Facility and Innovative Instrument Project (AS-CFII108-113) for cell sorting service. We thank Inflammation Core Facility of Institute of Biomedical Sciences, Academia Sinica for multiplexed murine cytokine test. The Lai Lab is supported by Ministry of Science and Technology (MOST) grants 104-2320-B-007-005-MY2 (C.P.L.), 106-2320-B-007-004-MY3 (C.P.L.), Academia Sinica Innovative Materials and Analysis Technology Exploration (i-MATE) Program AS-iMATE-107-33 (C.P.L.), and Academia Sinica Career Development Award AS-CDA-109-M04 (C.P.L.).

Contributions

A.Y.W. and C.P.L. conceived and designed the study. A.Y.W., J.J.K. and A.L.A. performed initial experiments. A.Y.W., V.G., J.C.C., J.C.C. and H.W. performed characterization experiments. A.Y.W., Y.C.S., H.C.H. and Y.C. performed animal studies. S.T.C. and K.U. performed and analyzed proteomic study. M.R.H. performed and analyzed proteomic AF4 experiment. M.E. performed and analyzed TEM imaging. A.Y.W., V.G. and C.P.L. analyzed data. C.H.Y.C. and H.F.J. help proteomics analysis and data processing. W.W.L. and C.P.L. supervised the study. The manuscript was written by A.Y.W. and C.P.L. with input from all authors.

Competing interests

The authors declare no competing interests.

References

1. Yáñez-Mó, M. et al. Biological properties of extracellular vesicles and their physiological functions. *Journal of Extracellular Vesicles* **4** (2015).
2. Zaborowski, M.P., Balaj, L., Breakefield, X.O. & Lai, C.P. Extracellular Vesicles: Composition, Biological Relevance, and Methods of Study. *Bioscience* **65**, 783-797 (2015).
3. Wu, A.Y., Ueda, K. & Lai, C.P. Proteomic Analysis of Extracellular Vesicles for Cancer Diagnostics. *Proteomics* **19**, e1800162 (2019).
4. Zhang, H. et al. Identification of distinct nanoparticles and subsets of extracellular vesicles by asymmetric flow field-flow fractionation. *Nat Cell Biol* **20**, 332-343 (2018).
5. Théry, C. et al. Minimal information for studies of extracellular vesicles 2018 (MISEV2018): a position statement of the International Society for Extracellular Vesicles and update of the MISEV2014 guidelines.

Journal of Extracellular Vesicles **7** (2018).

6. Tkach, M. & Thery, C. Communication by Extracellular Vesicles: Where We Are and Where We Need to Go. *Cell* **164**, 1226-1232 (2016).
7. Robbins, P.D. & Morelli, A.E. Regulation of immune responses by extracellular vesicles. *Nat Rev Immunol* **14**, 195-208 (2014).
8. Coleman, B.M. & Hill, A.F. Extracellular vesicles--Their role in the packaging and spread of misfolded proteins associated with neurodegenerative diseases. *Semin Cell Dev Biol* **40**, 89-96 (2015).
9. Reiner, A.T. et al. Concise Review: Developing Best-Practice Models for the Therapeutic Use of Extracellular Vesicles. *Stem Cells Transl Med* **6**, 1730-1739 (2017).
10. Shao, H. et al. New Technologies for Analysis of Extracellular Vesicles. *Chem Rev* **118**, 1917-1950 (2018).
11. Hoshino, A. et al. Tumour exosome integrins determine organotropic metastasis. *Nature* **527**, 329-335 (2015).
12. Alvarez-Erviti, L. et al. Delivery of siRNA to the mouse brain by systemic injection of targeted exosomes. *Nat Biotechnol* **29**, 341-345 (2011).
13. Chuo, S.T., Chien, J.C. & Lai, C.P. Imaging extracellular vesicles: current and emerging methods. *J Biomed Sci* **25**, 91 (2018).
14. Ohno, S. et al. Systemically injected exosomes targeted to EGFR deliver antitumor microRNA to breast cancer cells. *Mol Ther* **21**, 185-191 (2013).
15. Morales-Kastresana, A. et al. Labeling Extracellular Vesicles for Nanoscale Flow Cytometry. *Sci Rep* **7**, 1878 (2017).
16. Peinado, H. et al. Melanoma exosomes educate bone marrow progenitor cells toward a pro-metastatic phenotype through MET. *Nat Med* **18**, 883-891 (2012).
17. Puzar Dominkus, P. et al. PKH26 labeling of extracellular vesicles: Characterization and cellular internalization of contaminating PKH26 nanoparticles. *Biochim Biophys Acta Biomembr* **1860**, 1350-1361 (2018).
18. Rieck, B. Unexpected durability of PKH 26 staining on rat adipocytes. *Cell Biol Int* **27**, 445-447 (2003).
19. Takahashi, Y. et al. Visualization and in vivo tracking of the exosomes of murine melanoma B16-BL6 cells in mice after intravenous injection. *J Biotechnol* **165**, 77-84 (2013).
20. Lai, C.P. et al. Dynamic biodistribution of extracellular vesicles in vivo

using a multimodal imaging reporter. *ACS Nano* **8**, 483-494 (2014).

21. De, A., Jasani, A., Arora, R. & Gambhir, S.S. Evolution of BRET Biosensors from Live Cell to Tissue-Scale In vivo Imaging. *Front Endocrinol (Lausanne)* **4**, 131 (2013).

22. Schaub, F.X. et al. Fluorophore-NanoLuc BRET Reporters Enable Sensitive In Vivo Optical Imaging and Flow Cytometry for Monitoring Tumorigenesis. *Cancer Res* **75**, 5023-5033 (2015).

23. England, C.G., Ehlerding, E.B. & Cai, W. NanoLuc: A Small Luciferase Is Brightening Up the Field of Bioluminescence. *Bioconjug Chem* **27**, 1175-1187 (2016).

24. Chu, J. et al. A bright cyan-excitable orange fluorescent protein facilitates dual-emission microscopy and enhances bioluminescence imaging in vivo. *Nat Biotechnol* **34**, 760-767 (2016).

25. Yeh, H.W. et al. Red-shifted luciferase-luciferin pairs for enhanced bioluminescence imaging. *Nat Methods* **14**, 971-974 (2017).

26. Mittelbrunn, M. et al. Unidirectional transfer of microRNA-loaded exosomes from T cells to antigen-presenting cells. *Nat Commun* **2**, 282 (2011).

27. Pilz, G.A. et al. Live imaging of neurogenesis in the adult mouse hippocampus. *Science* **359**, 658-662 (2018).

28. Lai, C.P. et al. Visualization and tracking of tumour extracellular vesicle delivery and RNA translation using multiplexed reporters. *Nat Commun* **6**, 7029 (2015).

29. Weigelin, B., Bakker, G.J. & Friedl, P. Third harmonic generation microscopy of cells and tissue organization. *J Cell Sci* **129**, 245-255 (2016).

30. You, S. et al. Intravital imaging by simultaneous label-free autofluorescence-multiharmonic microscopy. *Nat Commun* **9**, 2125 (2018).

31. Hwang, D.W. et al. Noninvasive imaging of radiolabeled exosome-mimetic nanovesicle using Tc-99m-HMPAO. *Sci Rep-Uk* **5** (2015).

32. Smyth, T. et al. Biodistribution and delivery efficiency of unmodified tumor-derived exosomes. *J Control Release* **199**, 145-155 (2015).

33. el-Husseini Ael, D. & Bredt, D.S. Protein palmitoylation: a regulator of neuronal development and function. *Nat Rev Neurosci* **3**, 791-802 (2002).

34. Gustafsson, N. et al. Fast live-cell conventional fluorophore nanoscopy with ImageJ through super-resolution radial fluctuations. *Nat Commun*

7, 12471 (2016).

35. Aicart-Ramos, C., Valero, R.A. & Rodriguez-Crespo, I. Protein palmitoylation and subcellular trafficking. *Biochim Biophys Acta* **1808**, 2981-2994 (2011).

36. Al-Nedawi, K. et al. Intercellular transfer of the oncogenic receptor EGFRvIII by microvesicles derived from tumour cells. *Nat Cell Biol* **10**, 619-624 (2008).

37. Corso, G. et al. Systematic characterization of extracellular vesicle sorting domains and quantification at the single molecule - single vesicle level by fluorescence correlation spectroscopy and single particle imaging. *J Extracell Vesicles* **8**, 1663043 (2019).

38. Kowal, J. et al. Proteomic comparison defines novel markers to characterize heterogeneous populations of extracellular vesicle subtypes. *Proc Natl Acad Sci U S A* **113**, E968-977 (2016).

39. Esser, J. et al. Exosomes from human macrophages and dendritic cells contain enzymes for leukotriene biosynthesis and promote granulocyte migration. *J Allergy Clin Immunol* **126**, 1032-1040, 1040 e1031-1034 (2010).

40. Tannous, B.A., Kim, D.E., Fernandez, J.L., Weissleder, R. & Breakefield, X.O. Codon-optimized Gaussia luciferase cDNA for mammalian gene expression in culture and in vivo. *Mol Ther* **11**, 435-443 (2005).

41. Hall, M.P. et al. Engineered luciferase reporter from a deep sea shrimp utilizing a novel imidazopyrazinone substrate. *ACS Chem Biol* **7**, 1848-1857 (2012).

42. Schindelin, J. et al. Fiji: an open-source platform for biological-image analysis. *Nat Methods* **9**, 676-682 (2012).

43. Alvarez-Erviti, L. et al. Lysosomal dysfunction increases exosome-mediated alpha-synuclein release and transmission. *Neurobiol Dis* **42**, 360-367 (2011).

44. Reiberger, T. et al. An orthotopic mouse model of hepatocellular carcinoma with underlying liver cirrhosis. *Nat Protoc* **10**, 1264-1274 (2015).

45. Feghali, C.A. & Wright, T.M. Cytokines in acute and chronic inflammation. *Front Biosci* **2**, d12-d26 (1997).

46. UniProt, C. UniProt: a worldwide hub of protein knowledge. *Nucleic Acids Res* **47**, D506-D515 (2019).

47. Haraguchi, N. et al. CD13 is a therapeutic target in human liver cancer

stem cells. *J Clin Invest* **120**, 3326-3339 (2010).

48. Megger, D.A. et al. Proteomic differences between hepatocellular carcinoma and nontumorous liver tissue investigated by a combined gel-based and label-free quantitative proteomics study. *Mol Cell Proteomics* **12**, 2006-2020 (2013).

49. Wlcek, K. et al. The analysis of organic anion transporting polypeptide (OATP) mRNA and protein patterns in primary and metastatic liver cancer. *Cancer Biol Ther* **11**, 801-811 (2011).

50. Centonze, M., Saponaro, C. & Mangia, A. NHERF1 Between Promises and Hopes: Overview on Cancer and Prospective Openings. *Transl Oncol* **11**, 374-390 (2018).

51. Zhu, Q., Liang, X., Dai, J. & Guan, X. Prostaglandin transporter, SLCO2A1, mediates the invasion and apoptosis of lung cancer cells via PI3K/AKT/mTOR pathway. *Int J Clin Exp Pathol* **8**, 9175-9181 (2015).

52. Yue, X., Cui, Y., You, Q., Lu, Y. & Zhang, J. MicroRNA124 negatively regulates chloride intracellular channel 1 to suppress the migration and invasion of liver cancer cells. *Oncol Rep* **42**, 1380-1390 (2019).

53. Zhang, S. et al. Chloride intracellular channel 1 is overexpression in hepatic tumor and correlates with a poor prognosis. *APMIS* **121**, 1047-1053 (2013).

54. Leenen, P.J. et al. Heterogeneity of mouse spleen dendritic cells: in vivo phagocytic activity, expression of macrophage markers, and subpopulation turnover. *J Immunol* **160**, 2166-2173 (1998).

55. Ghosh, M. et al. Molecular mechanisms regulating CD13-mediated adhesion. *Immunology* **142**, 636-647 (2014).

56. Campeau, E. et al. A versatile viral system for expression and depletion of proteins in mammalian cells. *PloS one* **4**, e6529 (2009).

57. Zhang, H. & Lyden, D. Asymmetric-flow field-flow fractionation technology for exomere and small extracellular vesicle separation and characterization. *Nat Protoc* **14**, 1027-1053 (2019).

58. Edelstein, A.D. et al. Advanced methods of microscope control using muManager software. *J Biol Methods* **1** (2014).

59. Cox, J. & Mann, M. MaxQuant enables high peptide identification rates, individualized p.p.b.-range mass accuracies and proteome-wide protein quantification. *Nat Biotechnol* **26**, 1367-1372 (2008).

60. Cox, J. et al. Andromeda: a peptide search engine integrated into the MaxQuant environment. *J Proteome Res* **10**, 1794-1805 (2011).

Figure 1. PalmGRET labels cellular and EV membranes. (a) Representation of multimodal PalmGRET labelling the inner leaflet of the plasma membrane of cells and EVs to emit BLI and FL using BRET excitation (BRET-FL), as well as FL from external light excitation. **(b)** Lentiviral constructs for PalmGRET and GRET (control) for EV labelling. **(c)** Multi-resolution EV imaging. PalmGRET labels cellular membranes to enable imaging of EV donor cells and EVs from nanoscopic to macroscopic resolutions by FL and/or BLI signals. **(d)** 3D reconstruction of Z-stack, live-cell confocal micrographs of 293T-PalmGRET cells, revealing uneven, budding membrane surfaces (arrows) and protrusions (arrowheads) that may be precursors of EV release. **(e)** Co-culture of 293T-PalmGRET and 293T-PalmtdTomato cells showing released EVs in the extracellular space. 293T-PalmGRET EV (arrows); 293T-PalmtdTomato EVs (arrowheads). Bar, 40 μm.

Figure 2. PalmGRET labels inner EV membrane and exhibits robust BLI signals in EVs. (a, b) Nanoparticle tracking analysis of EV-wildtype (WT), EV-GRET and EV-PalmGRET, demonstrating their similar **(a)** size distributions (peaks at 111, 112 and 121 nm, respectively; representative data of three independent experiments) and **(b)** mean sizes (determined from four independent experiments). One-way ANOVA followed by Tukey's *post hoc* test was used. N.S., non-significant with $p > 0.05$. **(c, d)** Transmission electron micrographs showing that PalmGRET labels EVs at their membranes. Micrographs of isolated EV-293T-PalmGRET and EV-293T-GRET

immunogold labelled with **(c)** anti-GFP or **(d)** anti-CD63, and secondary gold-conjugated secondary antibodies. Bar, 100 nm. **(e, f)** Dot blot analysis showing that PalmGRET labels the EV inner membrane. A strong PalmGRET signal was only detected in the presence of **(f)** Tween-20 detergent [0.1% (v/v)] in a dose-dependent manner when compared with **(e)** the GRET control, thereby indicating inner EV membrane-specific labelling by PalmGRET. Cell lysates were applied as positive controls. **(g, h)** Nluc activity assay of EV-293T-PalmGRET and EV-293T-GRET following **(g)** sucrose gradient fractionation and **(h)** fraction pelleting. A significantly higher Nluc activity was detected in EV-containing fractions (Nos. 3-6) of EV-PalmGRET-EV when compared to that of EV-293T-GRET. **(i)** Western blot analysis of EV proteins isolated from the pelleted fractions revealed that PalmGRET (right), but not GRET (left), coincides with Alix (95 kDa) and CD63 (30–60 kDa). Cell lysates of 293T-PalmGRET and 293T-GRET were applied as positive controls. The expected sizes of PalmGRET and GRET are 49 and 46 kDa, respectively.

Figure 3. PalmGRET labels multiple bionanoparticle populations and exhibits long-term reporter signals in EVs. (a) AF4 analysis of bionanoparticles isolated from stable 293T-PalmGRET and 293T-GRET cells. PalmGRET appears to increase the size of exomeres (P2) but not Exo-S (P3) or Exo-L (P4) when compared with the control (GRET). Scattered dots represent the hydrodynamic radii of detected particles. The blue solid line indicates relative particle abundance detected using UV (280 nm) light. The red solid line represents particle abundance detected by quasi-elastic light scattering (QELS) detection. **(b, c)** Nluc and BRET activities of AF4 fractionated bionanoparticles indicating pan-labelling by PalmGRET. Thus labelled bionanoparticles showed 10-times higher **(b)** BLI and **(c)** BRET-FL signals in exomere, Exo-S and Exo-L fractions than the control (GRET). The resulting BLI and BRET-FL activities of different subpopulations were normalized to the volume of concentrate from the Amicon Ultra-15 30-kDa molecular weight cut-off concentration. N.S., $p > 0.05$; **/ ##, $p < 0.01$; ***/ ###, $p < 0.001$ with one-way ANOVA followed by Tukey's *post hoc* test. **(d–h)** Nluc and BRET activity analyses revealed that EV-PalmGRET emits strong and sustained **(d)** BLI and **(e)** BRET-GFP signals. **(f)** Both EV-293T-PalmGRET and EV-293T-GRET exhibited a similar BRET ratio, suggesting that BRET efficiency is not affected by the palmitoylation moiety in EV-293T-PalmGRET. While EV-GRET showed a longer half-life, EV-PalmGRET exhibited greater AUCs in its emitted **(g)** Nluc and **(h)** BRET-FL signals during four independent experiments. **RFU**, relative fluorescence unit; **RLU**, relative light unit. *, $p < 0.05$; **, $p < 0.01$ with two-tailed Student's t-test.

Figure 4. PalmGRET enables super-resolution fluorescence imaging of EVs *in vivo* and *ex vivo*. (a) Live-cell, fluorescence imaging of 293T-PalmGRET cells. Cells were imaged by epifluorescence and SRRF microscopy under 488 nm excitation to detect cellular and EV expression of PalmGRET. PalmGRET enables super-resolution imaging of EVs by SRRF microscopy as demonstrated by the comparative micrographs imaged by SRRF (top) and epifluorescence microscopy (bottom) of the boxed regions (i, ii). Individual EVs (arrows) can be resolved in the (i) extracellular space and (ii) cell periphery by SRRF imaging. Epifluorescence microscopy bar, 10 μm; SRRF nanoscopy bar, 1 μm. **(b)** Top, live-cell SRRF imaging of 293T-PalmGRET cells and released EVs. Bar, 1 μm. Bottom, enlarged image of the boxed region exhibiting released EVs. Bar, 200 nm. **(c)** Time-lapse live-cell SRRF imaging of 293T-PalmGRET cells showing a EV protrusion-like event. Bar, 200 nm. See also **Supplementary Movies 2 and 3. (d)** SRRF imaging of lung sections 30 min post-injection of 100 μg EV-293T-PalmGRET or PBS (control). The administered EVs can be detected by SRRF nanoscopy (arrow). The nuclei were stained by DAPI, and EV-293T-PalmGRET was immunoprobed by anti-GFP antibody followed by AlexaFluor 568-secondary antibody. Enlarged images (dashed boxes) of the boxed regions are placed at top right corner. Bar, 10 μm.

Figure 5. PalmGRET enables multimodal, multi-resolution imaging and analysis of EVs' distribution in organs. (a) Schematic of *in vivo* time-lapsed imaging of EVs. Immunocompetent C3H mice were administered with EV-293T-PalmGRET (100 μg) into the tail vein followed by Fz injection for *in vivo* imaging at 5, 10, 20 and 30 min post-EV administration. **(b)** Bolus IV-injected EV-293T-PalmGRET (100 μg) was visualized under BLI and BRET-FL (GFP using BRET) channels from 5 to 20 min post-administration. The majority of the EV signals were detected at the lungs and spleen. By contrast, imaging under epi-illumination resulted in mostly scattered, non-EV-specific signals. **(c)** *Ex vivo* imaging of organs harvested at 30 min post-injection of EV-293T-PalmGRET (100 μg) (Mice Nos. 1 and 2) and WT subjects. EV-293T-PalmGRET signals were readily detected in the lungs, liver and spleen. **(d)** SRRF nanoscopy of lung sections at 30 min post-injection of EV-293T-PalmGRET (100 μg) or PBS (control). Enlarged images (dashed boxes) of boxed regions (i, ii) reveal injected EVs in lung tissues. The nuclei were stained by DAPI, and EV-293T-PalmGRET was immunoprobed by anti-GFP antibody followed by AlexaFluor 568-secondary antibody to minimize background signal. Bar, 10 μm; in enlarged images, 500 nm. **(e)** Quantification of EV signals by SRRF imaging demonstrated a significant increase in EV counts in the lungs followed by the spleen and liver at 30 min post-EV injection. The kidneys showed no significant increase in EV counts.

293T-PalmGRET signals were quantified by ImageJ from seventy images of tissue sections of mice injected with EV-293T-PalmGRET or PBS. The EV counts were normalized against organ weight. N.S., $p > 0.05$; *, $p < 0.05$; **, $p < 0.01$ with two-tailed Student's t-test.

Figure 6. Lung-tropic redirection of EVs yields distinct organ distribution profiles. (a) Schematic for tracking spontaneous lung metastasis of orthotopically implanted hepatocellular carcinoma HCA-1 in C3H immunocompetent mice. **(b)** Left, *in vivo* imaging under BLI and BRET-FL to visualize liver tumour progression. Right, *ex vivo* imaging of collected organs showing tumours in the livers, as well as lung metastasis. Very low levels of signals were detected at the spleen and intestine. **(c)** Schematic for EV-tropism experiment. C3H mice were IV administered with EV-HCA-1-PalmGRET (30 μg) or EV-293T-PalmGRET (30 μg) at 0, 24, 48 and 72 h. The organs were harvested at 0.5 and 72.5 h for organ distribution analysis. **(d)** Organ distribution analysis revealed lung-tropism of EV-HCA-1-PalmGRET when compared with EV-293T-PalmGRET following EV education. $N = 3$ mice per group with technical triplicates. Percentages for each organ at different time points were acquired by $\frac{Mean\ RLU\ (Organ)}{\Sigma\ of\ Mean\ ELU(All\ organs)}$.*, $p < 0.05$; **, $p < 0.01$; ***, $p < 0.001$; ****, $p < 0.0001$ with two-tailed Student's t-test. **(e)** Schematic for lung-tropic redirection of EVs. 293T-PalmGRET cells were transfected with mock (WT) or plasmids encoding lung-tropic protein candidates followed by EV isolation. C3H mice were IV administered with the EVs (10 μg) at 0, 24, 48 and 72 h, and organs were collected for organ distribution analysis at 0.5 and 72.5 h. **(f)** Spatially resolved EV-organ dynamics reveal an inverse distribution of EVs between the lungs and liver following lung-tropic redirection. Three of the five lung-tropic EV protein candidates (CLIC1, and SLCO2A1) redirected EV-293T-PalmGRET to the lungs when compared with the WT control. By contrast, the three proteins decreased EV distribution to the liver. Percentages for each organ at different time points were acquired by $\frac{Mean\ RLU\ (Organ)}{\Sigma\ of\ Mean\ ELU(All\ organs)}$. *, $p < 0.05$; **, $p < 0.01$; ***, $p < 0.001$; ****, $p < 0.0001$ with one-way ANOVA followed by Dunnett's *post hoc* test compared with the WT. $N = 3$ mice per group with technical triplicates. **(g)** List of lung-tropic EV protein candidates of hepatocellular carcinoma EVs. SLCO2A1, solute carrier organic anion transporter family member 2A1; NHERF1, sodium-hydrogen antiporter 3 regulator 1; CD13 (ANPEP), alanine aminopeptidase; CLIC1, chloride intracellular channel; OE, overexpression.

Supplementary Figure 1. Original Western blots of EV-GRET and EV-

PalmGRET following sucrose gradient purification. Nitrocellulose membranes (pore size: 0.45 μm) were cut to two blots to acquire Alix and CD63 signals on the first day. GFP of GRET/PalmGRET was detected the next day after treating the CD63 blot with stripping buffer and immunoprobing with anti-GFP antibody. Expected size: Alix (95 kDa), CD63 (30-60 kDa), GRET (46 kDa) and PalmGRET (49 kDa).

Supplementary Figure 2. Nluc and BRET activities of stable 293T-PalmGRET and 293T-GRET cells. (a) 293T-GRET cells (Cell-GRET) showed a higher Nluc activity from 0 to 60 min following Fz administration than either 293-PalmGRET cells (Cell-PalmGRET) or wildtype 293T cells (Cell-WT; control). Cell-WT exhibited a limited amount of Nluc background activity. **(b)** BRET-excited GFP fluorescence was simultaneously collected in the same experiment, and Cell-GRET demonstrated a higher amount of GFP signal using BRET than Cell-PalmGRET from 0 to 60 min. Cell-WT showed no detectable GFP signal. (**c**) Cell-PalmGRET and Cell-GRET exhibited a significantly higher and similar BRET ratio over time than Cell-WT control. **(d)** Half-life and AUC of Nluc. **(e)** Half-life and AUC of BRET-excited GFP. *, $p < 0.05$; **, $p < 0.01$ with two-tailed Student's t-test.

Supplementary Figure 3. PalmGRET labels small, medium and large EVs. Conditioned medium from 293T-PalmGRET cell were filtered with a 0.22, 0.8 or 1.2 μm filter to examine the labelling ability of EV subtypes by PalmGRET. 5 μL EVs from each group was used to record time-lapse data for **(a)** BLI, **(b)** BRET-FL and **(c)** BRET ratio. Representative charts from one of the three independent experiments are shown. Half-life and AUC of **(d)** BLI (half-lives for the 0.22, 0.8 and 1.2 μm samples were 8.3 ± 1.07, 7.93 ± 0.61 and 8.08 ± 0.62 min, respectively; their AUCs were 7.4 ± 1.58, 9.3 ± 1.69 and 11.4 ± 1.13 RLU·min/particles, respectively); and **(e)** BRET-FL (half-lives for the 0.22, 0.8 and 1.2 μm samples were 8.3 ± 1.06, 8.0 ± 0.60 and 8.07 ± 0.63 min, respectively; their AUCs were 15.4 ± 3.37, 19.3 ± 3.49 and 23.2 ± 2.35 RFU·min/particles, respectively) were calculated from (**a** and **b**). N.S., $p > 0.05$; *, $p < 0.05$ with one-way ANOVA followed by Tukey's *post hoc* test for three independent experiments. (**f, g**) 3 μL EV was used for SRRF nanoscopy and EV quantification. **(f)** SRRF nanoscopy of EV-293T-PalmGRET isolated from 0.22, 0.8 or 1.2 μm filtered CM. Bar, 500 nm. **(g)** Quantification of EVs from SRRF nanoscopy images demonstrates a positive correlation between EV count and filter pore sizes. Eight fields of interest were taken from EVs of three independent experiments ($N = 24$). **, $p < 0.01$; ***, $p < 0.001$; ****, $p < 0.0001$ with one-way ANOVA followed by Tukey's *post hoc* test.

Supplementary Figure 4. Live-cell, multimodal imaging of 293T-PalmGRET and

293T-GRET cells. The cells were treated with Fz and imaged by an EMCCD camera to detect BRET-excited GFP signals. Bar, 10 μm. The same samples were next imaged by epifluorescence (Bar, 10 μm) and SRRF (Bar, 1 μm) microscopy under 488 nm excitation to detect cellular and EV expression of PalmGRET.

Supplementary Figure 5. SRRF nanoscopy of organs from EV-293T-PalmGRET-administered C3H immunocompetent mice. SRRF and DIC images of spleen, liver, and kidney sections at 30 min post-EV-293T-PalmGRET (100 μg) or PBS (control) injection. DAPI was used for nucleus staining; primary anti-GFP and Alexa Fluor® 568-conjugated secondary antibodies were used to probe PalmGRET. Bar, 10 μm. Enlarged images (dashed boxes) of boxed region (i, ii) are placed at the top of the merged images. Bar, 500 nm.

Supplementary Figure 6. Mosaic SRRF images reveal an uneven distribution of EV-293T-PalmGRET in the lungs of C3H mice. 5 × 5 mosaic SRRF and DIC images of C3H mouse lung tissue injected with EV-293T-PalmGRET (top, 100 μg) and PBS (bottom). DAPI was used for nucleus staining; anti-GFP primary antibody followed by Alexa Fluor® 568-conjugated secondary antibody were used for PalmGRET staining. Bar, 50 μm. Enlarged images (dashed boxes) of boxed regions (i–iii) indicate detected EV or background signals (control). Bar, 500 nm.

Supplementary Figure 7. EV-HCA1-PalmGRET and EV-293T-PalmGRET exhibit a distinct organ distribution profile at 0.5 or 72.5 h post-IV administration. Pie charts demonstrating EV-HCA1-PalmGRET predominately localized to the lungs and liver, whereas EV-293T-PalmGRET mostly distributed to the spleen. This pattern is enhanced at 72.5 h post-EV education. Percentages for each organ at different time points were acquired by $\frac{Mean\ RLU\ (Organ)}{\Sigma\ of\ Mean\ ELU(All\ organs)}$. N = 3 mice per group.

Supplementary Figure 8. PalmGRET reports EV circulation time in C3H immunocompetent mice. 30 μg EV-HCA-1-PalmGRET was IV-injected into C3H mice's tail veins. At 5, 30 and 60 mins post-EV injection, blood was collected to isolate the plasma with EDTA as an anti-coagulant. Blood of PBS injected mice was collected at 5 min post-EV injection. Using qEVoriginal 70 nm columns to isolate EVs from the plasma, fractions Nos. 7–9 were collected for BLI activity assay. BLI activities are shown for **(a)** fraction pools and **(b)** individual fractions. The BLI activities of the fractions were normalized to the volume of concentrate following Amicon Ultra-0.5 with a 10-kDa molecular weight cut-off concentration. N = 1 mouse per time point with technical triplicates.

Supplementary Figure 9. Western blot analysis of 293T-PalmGRET cell and derived EVs overexpressing EV lung-tropism protein candidates. (a) NHERF1, sodium-hydrogen antiporter 3 regulator 1 (40 kDa); **(b) CLIC1**, chloride intracellular channel (27 kDa); **(c) CD13 (ANPEP)**, alanine aminopeptidase (110 kDa); **(d) SLCO2A1**, solute carrier organic anion transporter family member 2A1 (65 kDa). **GAPDH**, glyceraldehyde-3-phosphate dehydrogenase (34 kDa) as cell loading control; **ALIX**, ALG-2-interacting protein X (95 kDa) as EV marker.

Supplementary Figure 10. Organ distribution analysis of EV-293T-PalmGRET demonstrates EV-organ dynamics following redirected EV lung-tropism. Pie charts illustrating redirected lung distribution with an overall decrease in distribution to the liver of C3H mice educated with EV-293T-PalmGRET overexpressing either CLIC1 or SLCO2A1 compared with the WT. Percentages for each organ at different time points were acquired by $\frac{Mean\ RLU\ (Organ)}{\Sigma\ of\ Mean\ ELU(All\ organs)}$. N = 3 mice per group.

Supplementary Movie 1. 3D reconstruction of live-cell confocal Z-stack images of 293T-PalmGRET and 293T-PalmtdTomato co-culture.

Supplementary Movie 2. Live-cell SRRF nanoscopy of 293T-PalmGRET cells.

Supplementary Movie 3. Boxed region of Supplementary Movie 2 showing budding-like protrusion.

Supplementary Table 1. List of primers.

Supplementary Table 2. List of antibodies.

Supplementary Table 3. Trend comparison for organ distributions of EV-HCA1-PalmGRET and EV-293T-PalmGRET.

Supplementary Table 4. Cytokine profiles of C3H mice injected with EV-293T-PalmGRET- or EV-HCA-1-PalmGRET.

Supplementary Table 5. Proteomic data of EV-HCA-1-PalmGRET and EV-293T-PalmGRET.

Supplementary Table 6. Trend comparison for organ distributions of EV overexpressing lung-tropic protein candidates.

Figure 1

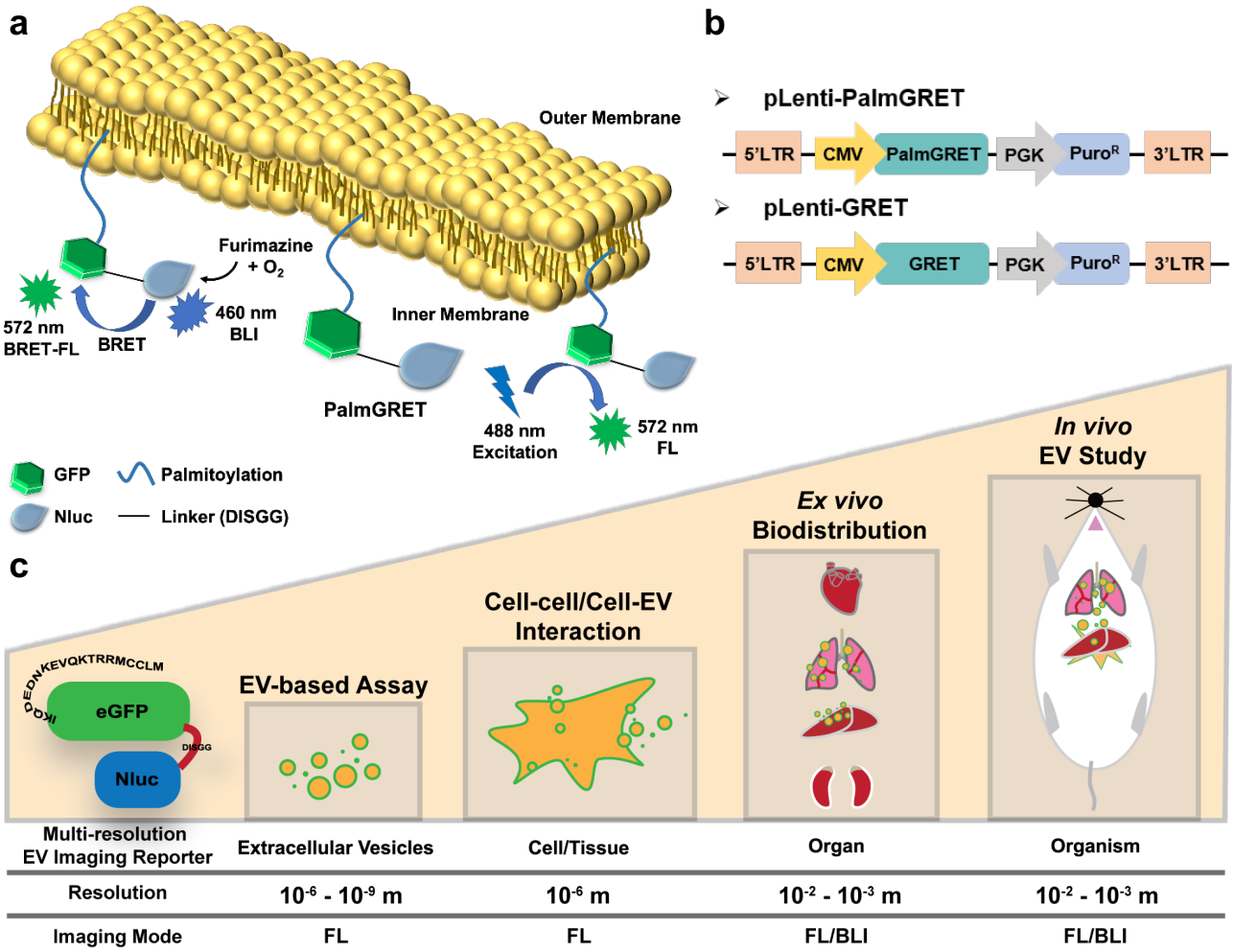
a
Outer Membrane
Furimazine
+ O_2
572 nm
BRET-FL
BRET
460 nm
BLI
Inner Membrane
PalmGRET
488 nm
Excitation
572 nm
FL
GFP
Palmitoylation
Nluc
Linker (DISGG)
b
pLenti-PalmGRET
5'LTR
CMV
PalmGRET
PGK
PuroR
3'LTR
pLenti-GRET
5'LTR
CMV
GRET
PGK
PuroR
3'LTR
c
DEQNKEVQKTRRMCCLM
eGFP
DISGG
Nluc
EV-based Assay
Cell-cell/Cell-EV
Interaction
Ex vivo
Biodistribution
In vivo
EV Study
Multi-resolution
EV Imaging Reporter
Extracellular Vesicles
Cell/Tissue
Organ
Organism
Resolution
10^{-6} - 10^{-9} m
10^{-6} m
10^{-2} - 10^{-3} m
10^{-2} - 10^{-3} m
Imaging Mode
FL
FL
FL/BLI
FL/BLI

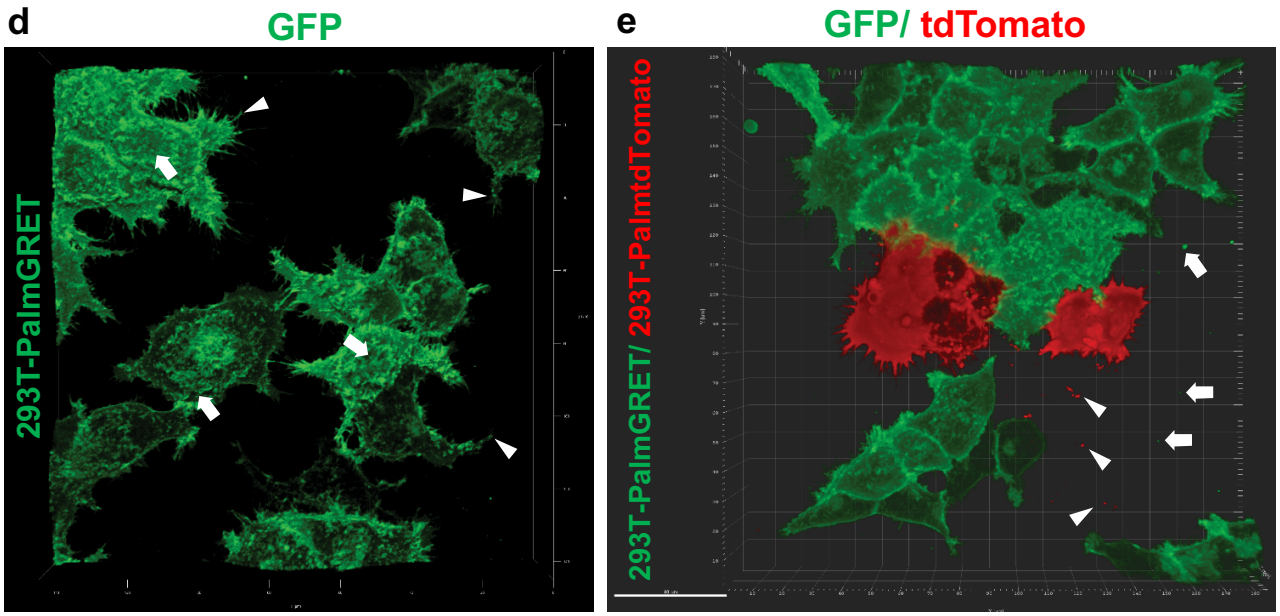
d
GFP
293T-PalmGRET
e
GFP/ tdTomato
293T-PalmGRET/ 293T-PalmtdTomato

Figure 2

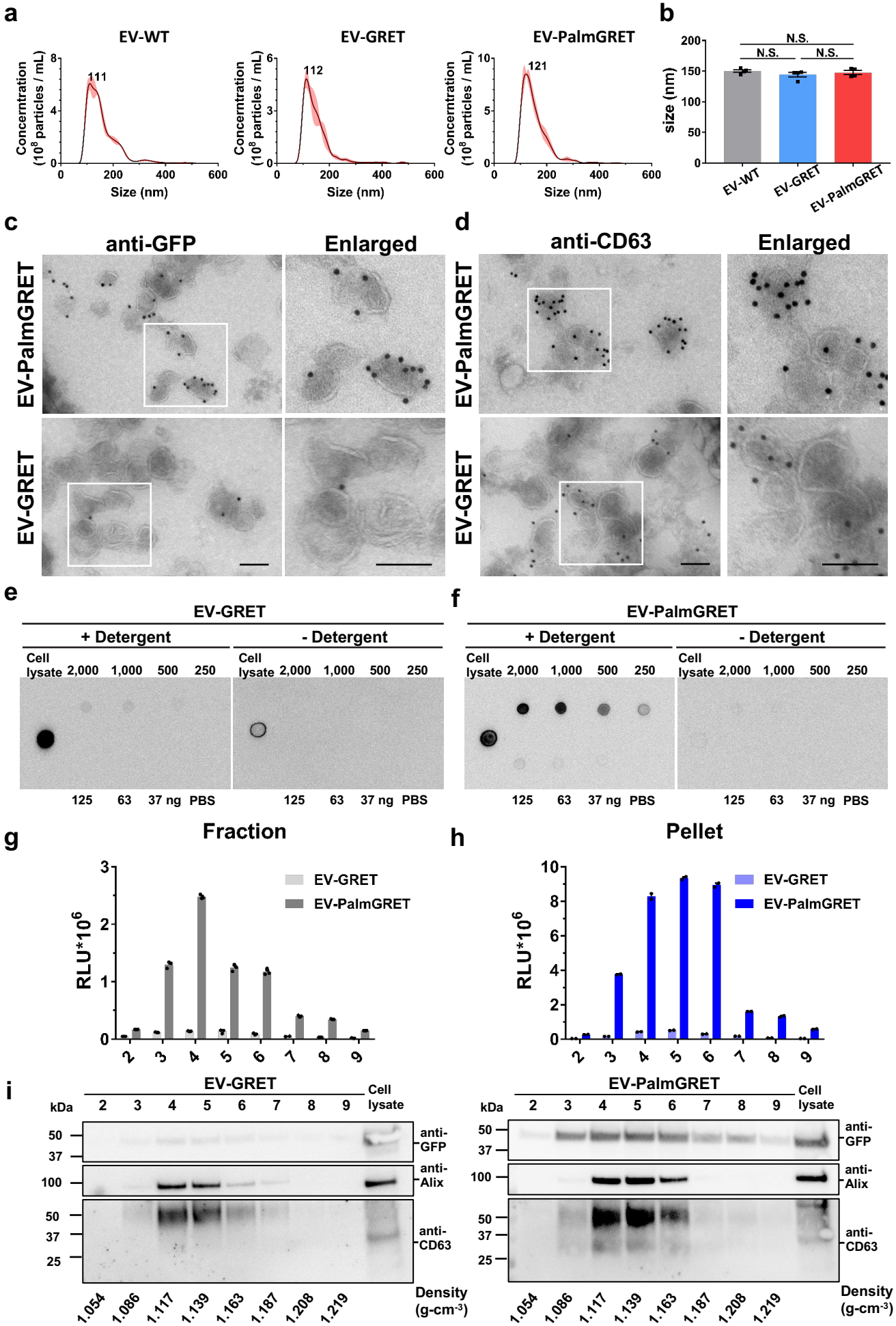
a
EV-WT
EV-GRET
EV-PalmGRET
Concentration (10^8 particles / mL)
Size (nm)
111
112
121
b
size (nm)
N.S.
EV-WT
EV-GRET
EV-PalmGRET
c
anti-GFP
Enlarged
EV-PalmGRET
EV-GRET
d
anti-CD63
Enlarged
e
EV-GRET
+ Detergent
- Detergent
Cell lysate
2,000
1,000
500
250
125
63
37 ng
PBS
f
EV-PalmGRET
g
Fraction
RLU*10^6
EV-GRET
EV-PalmGRET
h
Pellet
i
kDa
Cell lysate
anti-GFP
anti-Alix
anti-CD63
Density (g-cm^{-3})
1.054
1.086
1.117
1.139
1.163
1.187
1.208
1.219

Figure 3

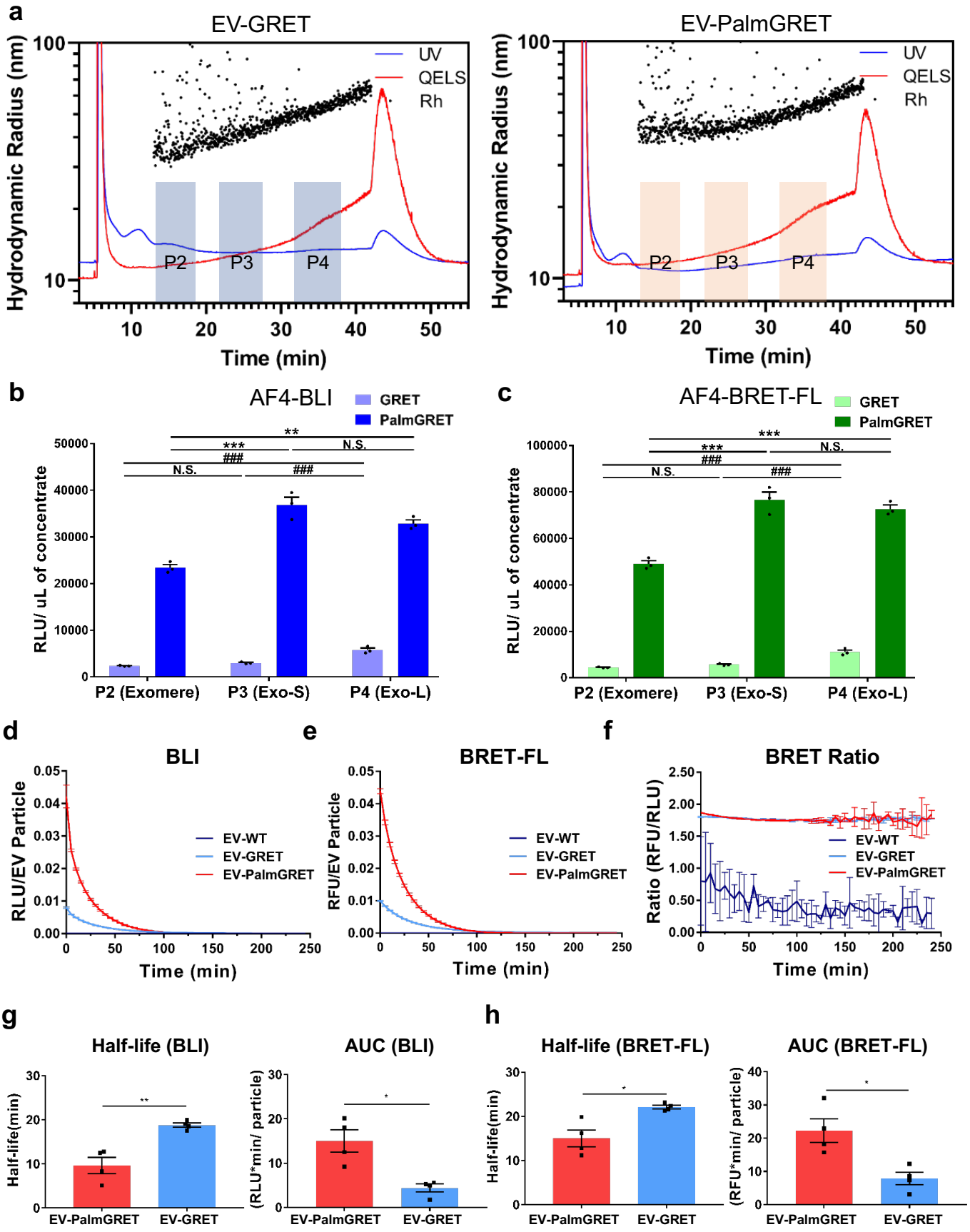
a
EV-GRET
EV-PalmGRET
Hydrodynamic Radius (nm)
Time (min)
UV
QELS
Rh
P2
P3
P4
b
AF4-BLI
GRET
PalmGRET
RLU/ uL of concentrate
P2 (Exomere)
P3 (Exo-S)
P4 (Exo-L)
N.S.
***
**
###
c
AF4-BRET-FL
d
BLI
RLU/EV Particle
EV-WT
EV-GRET
EV-PalmGRET
e
BRET-FL
RFU/EV Particle
f
BRET Ratio
Ratio (RFU/RLU)
g
Half-life (BLI)
Half-life(min)
AUC (BLI)
(RLU*min/ particle)
h
Half-life (BRET-FL)
AUC (BRET-FL)
(RFU*min/ particle)

Figure 4

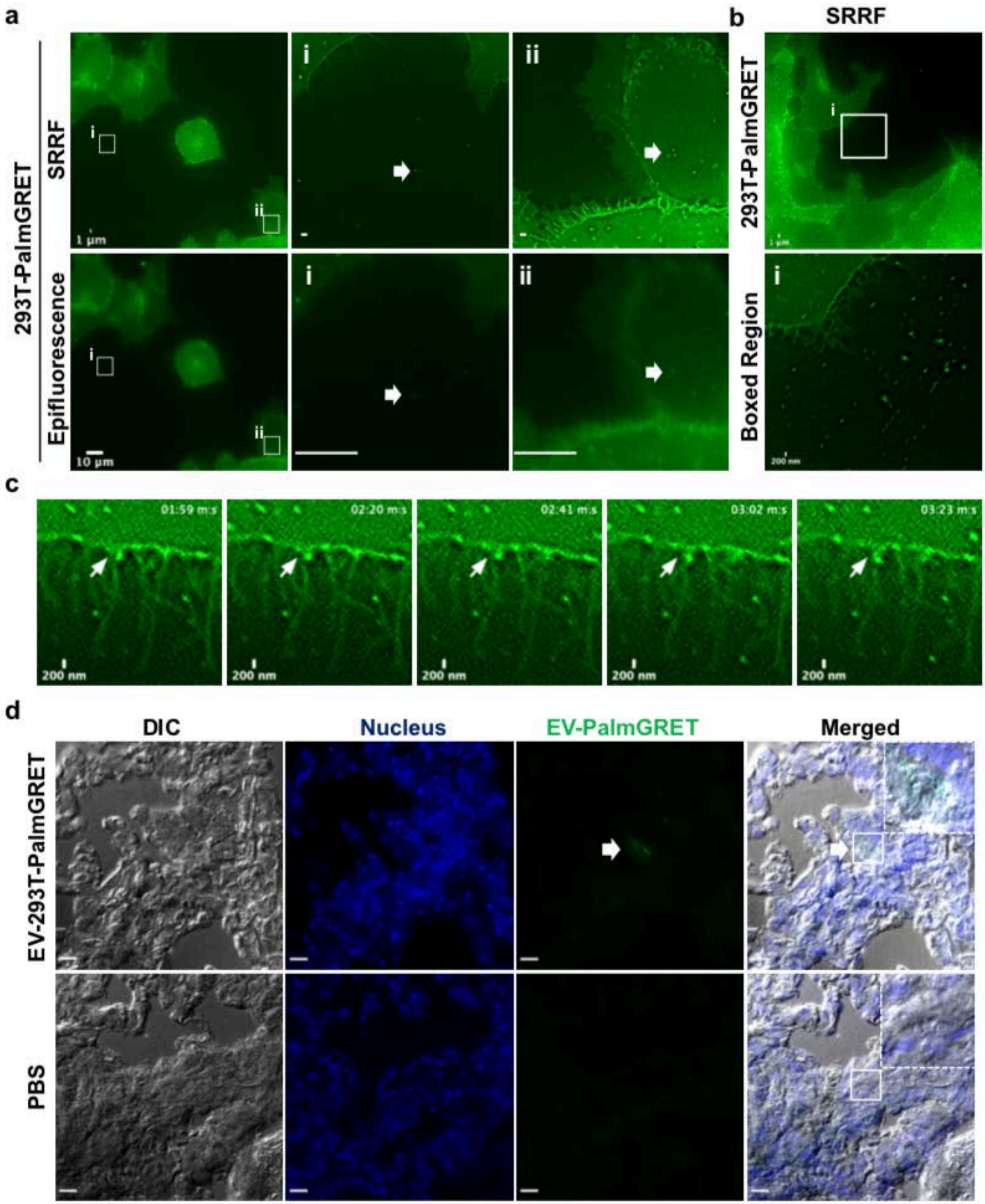
a
293T-PalmGRET
SRRF
Epifluorescence
i
ii
1 µm
10 µm
b
SRRF
293T-PalmGRET
Boxed Region
200 nm
c
01:59 m:s
02:20 m:s
02:41 m:s
03:02 m:s
03:23 m:s
200 nm
d
DIC
Nucleus
EV-PalmGRET
Merged
EV-293T-PalmGRET
PBS

Figure 5

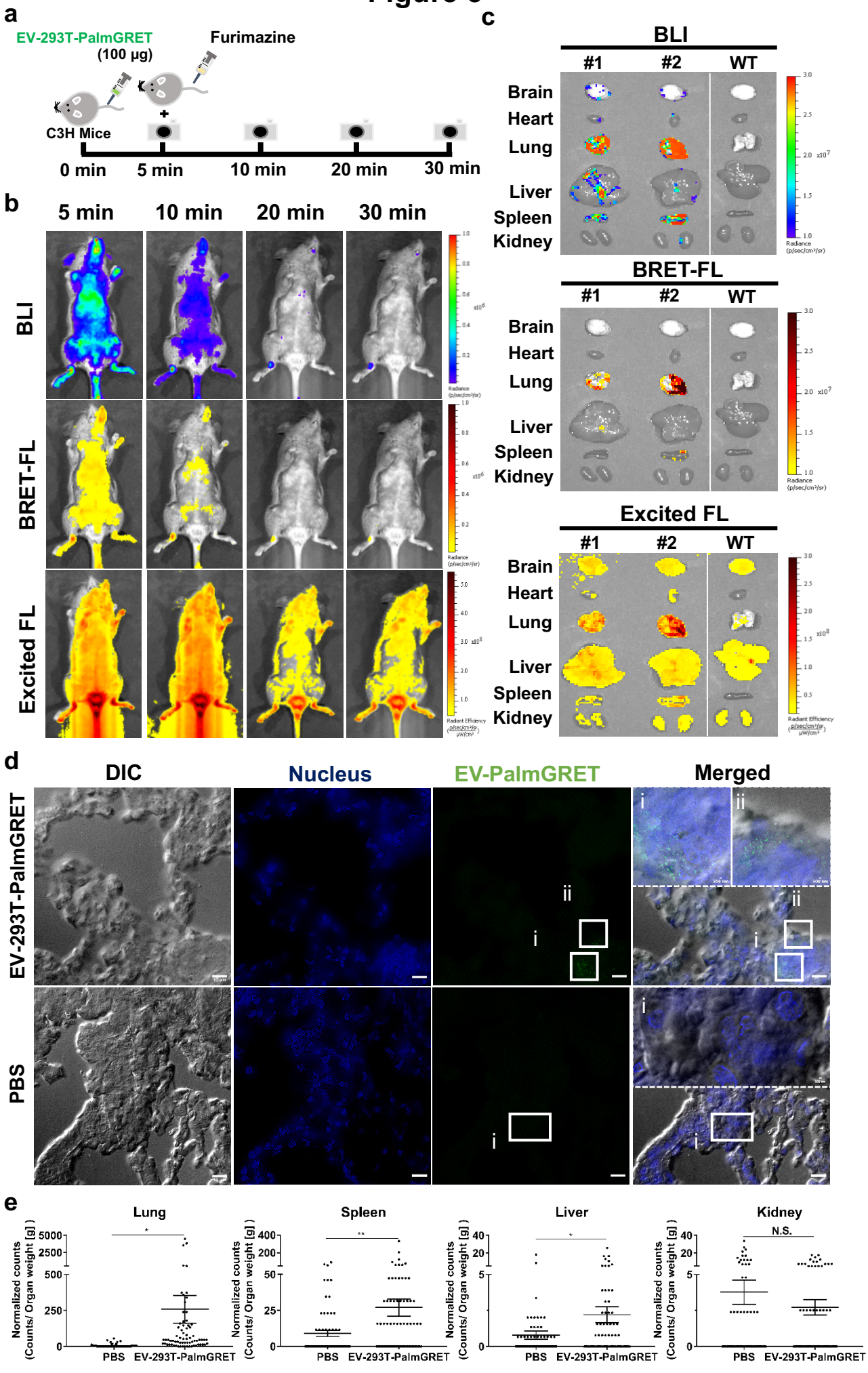
a
EV-293T-PalmGRET
(100 μg)
Furimazine
C3H Mice
0 min
5 min
10 min
20 min
30 min
b
5 min
10 min
20 min
30 min
BLI
BRET-FL
Excited FL
c
BLI
#1
#2
WT
Brain
Heart
Lung
Liver
Spleen
Kidney
BRET-FL
Excited FL
d
DIC
Nucleus
EV-PalmGRET
Merged
EV-293T-PalmGRET
PBS
e
Lung
Spleen
Liver
Kidney
Normalized counts
(Counts/ Organ weight [g])
PBS
EV-293T-PalmGRET
N.S.

Figure 6

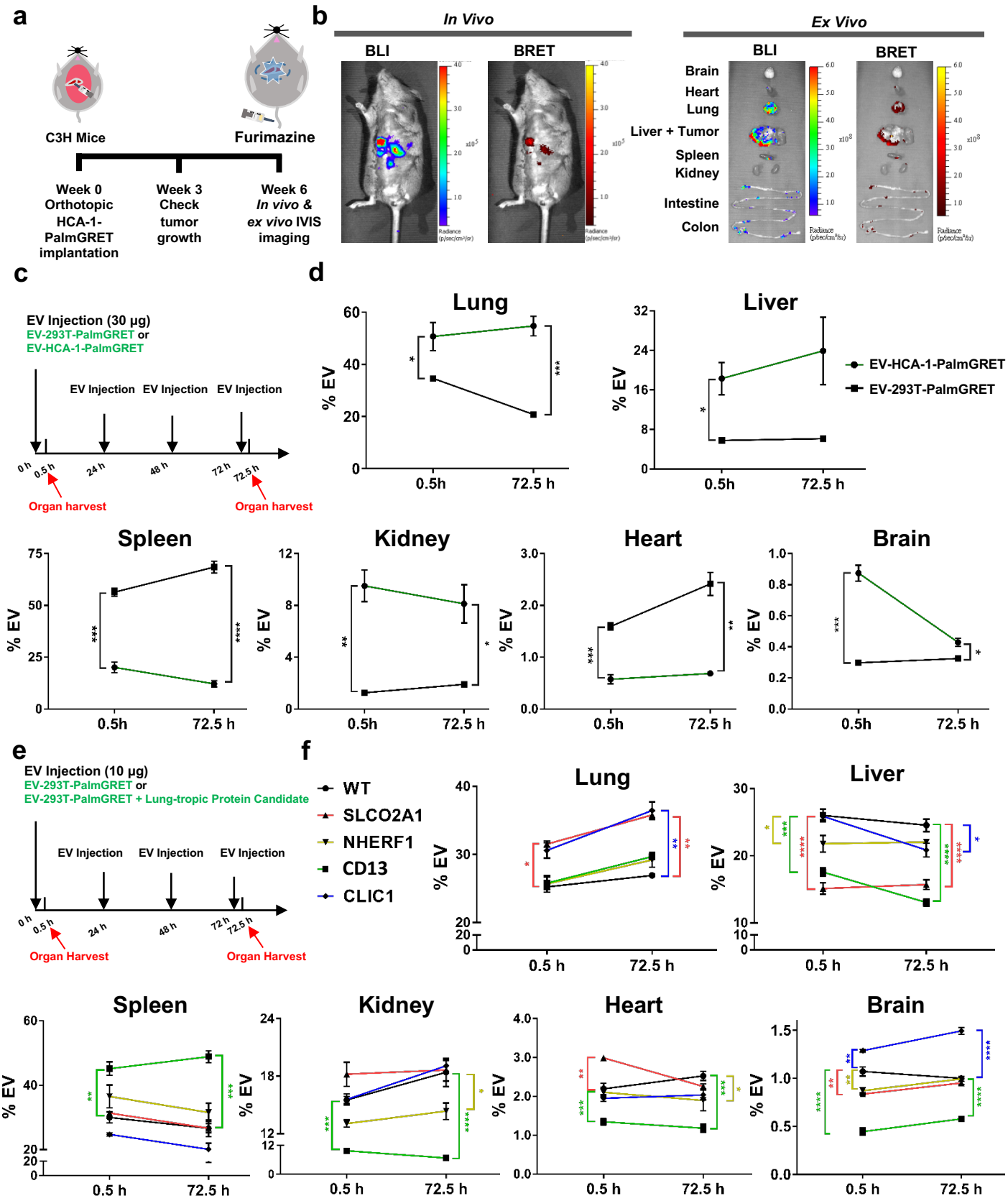

g

Protein ID	Protein	Function	Lung-tropism
P97449	CD13	HCC progression	Not Observed
Q9Z1Q5	CLIC1	HCC progression	Observed
P70441	NHERF1	Lung cancer progression	Not Observed
Q9EPT5	SLCO2A1	Metastatic hepatic tumor	Observed